bioRχiv

Aminergic and peptidergic modulation of Insulin-Producing Cells in *Drosophila*

Martina Held*[,1], Rituja S. Bisen*[,1], Meet Zandawala*[,2,3], Alexander S. Chockley[1], Isabella S. Balles[1], Selina Hilpert[2], Sander Liessem[1], Federico Cascino-Milani[1], and Jan M. Ache[1,#]

[1] Ache Lab, Neurobiology and Genetics, Theodor-Boveri-Institute, Biocenter, Julius-Maximilians-University of Würzburg, Am Hubland, 97074 Würzburg, Germany
[2] Zandawala Lab, Neurobiology and Genetics, Theodor-Boveri-Institute, Biocenter, Julius-Maximilians-University of Würzburg, Am Hubland, 97074 Würzburg, Germany
[3] Department of Biochemistry and Molecular Biology, University of Nevada Reno, Reno, 89557, NV, USA

* Equal contribution
[#] Lead contact, correspondence: jan.ache@uni-wuerzburg.de

Insulin plays a critical role in maintaining metabolic homeostasis. Since metabolic demands change momentarily, insulin release needs to be constantly adjusted. These adjustments are mediated via various pathways, most prominently the blood glucose level, but also by feedforward signals from motor circuits and different neuromodulatory pathways. Here, we analyzed how neuromodulatory inputs control the activity of the main source of insulin in *Drosophila* – a population of Insulin-Producing Cells (IPCs) located in the brain. IPCs are functionally analogous to mammalian pancreatic beta cells, but their location makes them accessible for *in vivo* recordings in intact animals. We characterized the functional inputs to IPCs using single-nucleus RNA sequencing analysis, anatomical receptor expression mapping, and an optogenetics-based "intrinsic pharmacology" approach. Our results showed that the IPC population expressed a variety of receptors for neuromodulators and classical neurotransmitters. Interestingly, individual IPCs exhibited heterogeneous receptor profiles, suggesting that they could be modulated differentially. This was supported by electrophysiological recordings of IPCs that we performed while activating different populations of modulatory neurons. Our analysis revealed that some modulatory inputs had heterogeneous effects on the IPC activity, such that they inhibited one subset of IPCs, while exciting another. Monitoring calcium activity across the IPC population uncovered that these heterogeneous responses occurred simultaneously. Certain neuromodulatory populations shifted the IPC population activity towards an excited state, while others shifted the IPCs towards inhibition. Taken together, we provide a comprehensive, multi-level framework of neuromodulation in the insulinergic system of *Drosophila*.

Introduction

Neuromodulation provides the foundation for neural circuit flexibility, which in turn facilitates adaptive behavioral and physiological responses to ever-changing internal demands and environmental conditions (Marder, 2012). Neuromodulators, such as neuropeptides and biogenic amines, regulate neural circuits through their diverse effects on neuronal excitability and synaptic transmission (Taghert & Nitabach, 2012; Nässel & Zandawala, 2022; Rosikon et al., 2023). Many neural circuits are targeted by multiple neuromodulators, which adds another layer of flexibility while also ensuring stability. Despite the importance of neuromodulation for brain and bodily functions, our understanding of the underlying mechanisms remains incomplete. This is largely due to a lack of *in vivo* model systems to investigate neuromodulation. Consequently, most studies to date used *ex vivo*, or reduced preparations, often investigating one modulatory system at a time (Marder, 2012; Daur et al., 2016). Here, we utilize Insulin-Producing Cells (IPCs), a group of approximately 14 neurosecretory cells in the pars intercerebralis of the *Drosophila* brain (Cao & Brown, 2001; Nässel & Vanden Broeck, 2016) as a model system to uncover principles of complex neuromodulation *in vivo*. This is particularly timely as recent advances of the *Drosophila* brain connectome provides an ideal platform to disentangle synaptic connections in an organism with a genetically accessible and numerically simple nervous system (Zheng et al., 2018; Scheffer et al., 2020; Dorkenwald et al., 2023). However, the connectome is based on synaptic connectivity and cannot be used to uncover paracrine connections, which are a hallmark of neuromodulation. IPCs are an ideal system to investigate principles of neuromodulation *in vivo* for several reasons: 1) IPCs release *Drosophila* insulin-like peptides (DILPs), which are analogous to human insulin. The insulin-signaling pathway and its functions are highly conserved across the animal kingdom, from worms to flies to humans (Prentki et al., 2013; Nässel & Vanden Broeck, 2016). For instance, insulin signaling is essential for many vital processes including metabolic homeostasis, feeding and foraging, ageing, and growth (Cao & Brown, 2001; Garofalo, 2002; Tatar et al., 2003; Partridge et al., 2011; Fernandez & Torres-Aleman, 2012; Nässel et al., 2013; Zandawala et al., 2018). Hence, the IPC activity and resultant insulin release needs to be carefully regulated on different timescales (Broughton et al., 2005;

Belgacem & Martin, 2006; Nässel, 2012; Liessem et al., 2023). 2) IPCs are modulated by different neuronal networks to adjust DILP release according to internal states, metabolic demands, and external inputs (Nässel et al., 2013; Nässel & Zandawala, 2020; Liessem et al., 2023). 3) IPCs have been characterized in the brain connectome, facilitating comparisons between modulatory and synaptic inputs (Reinhard et al., 2023). 4) The powerful genetic toolkit of *Drosophila* makes the IPCs not only accessible for *in vivo* recordings but also allows for simultaneous and controlled manipulation of other neuromodulatory populations via optogenetics, which permits an "intrinsic pharmacology" approach. 5) Their superficial location in the brain, in combination with genetic tools, enables IPC activity quantification *in vivo* with approaches like calcium imaging and whole cell patch-clamp recordings. Here, we used these advantages to unravel the dynamics of IPC modulation in *Drosophila*, providing a framework for understanding the regulation and possibly dysregulation of an insulinergic system. In humans, dysregulation of the homologous system underlies diabetes, obesity, and other metabolic disorders (Musselman et al., 2011; Ormazabal et al., 2018).

In *Drosophila*, all adult IPCs express DILP2, 3, and 5 and have traditionally been considered a homogeneous population (Broughton et al., 2005). However, emerging evidence has indicated that the IPCs could, in fact, represent a heterogeneous population. Specifically, only a subset of IPCs is intrinsically mechanosensitive via Piezo channels, which are required to prevent food overconsumption (Wang et al., 2020). In addition, recording the IPC responses to the stimulation of clock neurons or glucose revealed two to three subpopulations of IPCs (Oh et al., 2019; Barber et al., 2021). However, how individual IPCs are modulated by different neuronal pathways remains unclear. In this study, we employed an exhaustive, multi-level approach to leverage *Drosophila* IPCs as a model for understanding neuromodulatory dynamics and fundamental principles of metabolic homeostasis *in vivo*. Using a combination of single-nucleus transcriptome analyses, anatomical receptor mapping, optogenetics, whole cell patch-clamp recordings, and calcium imaging, we demonstrate that IPCs consist of at least 3 subpopulations. These subpopulations exhibited differential responses to the activation of modulatory neurons. At the molecular level, these heterogeneous responses of individual IPCs can largely be explained by differences in their expression profile of neuromodulator receptors. We hypothesize that this heterogeneity helps to buffer the system in a way that allows for an insulin release tailored to the ever-changing demands of the animal. In addition, we found that certain modulators shifted the overall activity of the IPC population towards excitation or inhibition, possibly to prime the system for higher or lower metabolic demands. Taken together, our work demonstrates that IPCs are part of a complex neuromodulatory network and integrate various regulatory inputs via different pathways. Furthermore, the regulatory motifs identified in our study regarding the orchestration by multiple modulatory systems, are likely also present in other modulatory systems, allowing for the generalization of our findings.

Results

Single-nucleus transcriptomic analysis identifies novel modulators of IPCs

Previous studies using a combination of molecular techniques, functional studies, and *ex vivo* recordings have shown that several neuropeptides, biogenic amines, and classical neurotransmitters modulate IPCs (Nässel & Vanden Broeck, 2016; Nässel & Zandawala, 2019, 2020). To identify additional novel modulators of IPCs and confirm previously published findings, we analyzed single-nucleus transcriptomes of IPCs, which were recently sequenced as part of the Fly Cell Atlas project (Li et al., 2022). Our analysis was based on 392 IPC transcriptomes, out of which 194 were derived from males and 198 from females. All these cells expressed *Ilp2, 3* and *5* (Figure S1A), the best-known marker genes for IPCs. *Drosulfakinin (Dsk)* neuropeptide, which has previously been shown to be expressed in a subset of IPCs (Söderberg et al., 2012; Wu et al., 2019), was very sparsely expressed in IPCs in this dataset (Figure S1A). This sparse expression was independently confirmed using a *Dsk-T2A-GAL4* knock-in line (Figure S1B). Nonetheless, high expression of all three *Ilp* transcripts in these cells confirmed that these transcriptomes were derived from IPCs.

To catalogue all modulators potentially involved in regulating IPC activity, we examined the expression of receptors for all biogenic amines and neuropeptides (Figure 1A) in IPC transcriptomes. Using a threshold of 5% expression, we found 22 neuropeptide and 17 biogenic amine receptors to be expressed in IPCs. This included receptors previously shown to be expressed in IPCs like *leucokinin receptor* (*Lkr*), *allatostatinA receptor 1* (*AstA-R1*), and the serotonin receptor *5-Hydroxytryptamine 1A* (5-*HT1A*) (Nässel & Zandawala, 2019, 2020; Sudhakar et al., 2020; Chatterjee & Perrimon, 2021) as well as several novel receptors, including *5-Hydroxytryptamine 7 (5-HT7)* and *5-Hydroxytryptamine 1B (5-HT1B) receptors*, *rickets (rk)*, *Trissin receptor (TrissinR)*, and others (Figure 1A). Since there were little differences in receptor expression between the two sexes (Figure S1C), we used the transcriptomes from both sexes for all subsequent analyses.

Interestingly, the insulin receptor (*InR*) was the highest expressed neuropeptide receptor in IPCs, suggesting that IPCs are modulated in an autocrine manner or by DILPs produced outside the IPCs. Moreover, IPCs express receptors for all classes of biogenic amines (Figure 1A). The *Drosophila* genome encodes multiple cognate receptors for all biogenic amines and some neuropeptides. Interestingly, multiple receptors for some of these ligands (e.g., all biogenic amines, Allatostatin-A (AstA) and Diuretic hormone 44 (DH44)) are expressed in IPCs. Since there are functional differences between different receptors for a given ligand (Larsen et al., 2001; Evans & Maqueira, 2005; Hector et al., 2009), co-expression of multiple receptors for a specific ligand in IPCs adds complexity to the modulatory input. In addition, IPCs can receive input via fast-acting, small molecule neurotransmitters since they express receptors for gamma-aminobutyric acid (GABA), glutamate (Glu) and acetylcholine (ACh; Figure S1D). Taken together, the gene expression data indicate that IPCs are intricately regulated by synaptic (via neurotransmitters) and paracrine/endocrine (via neuropeptides and biogenic amines) inputs.

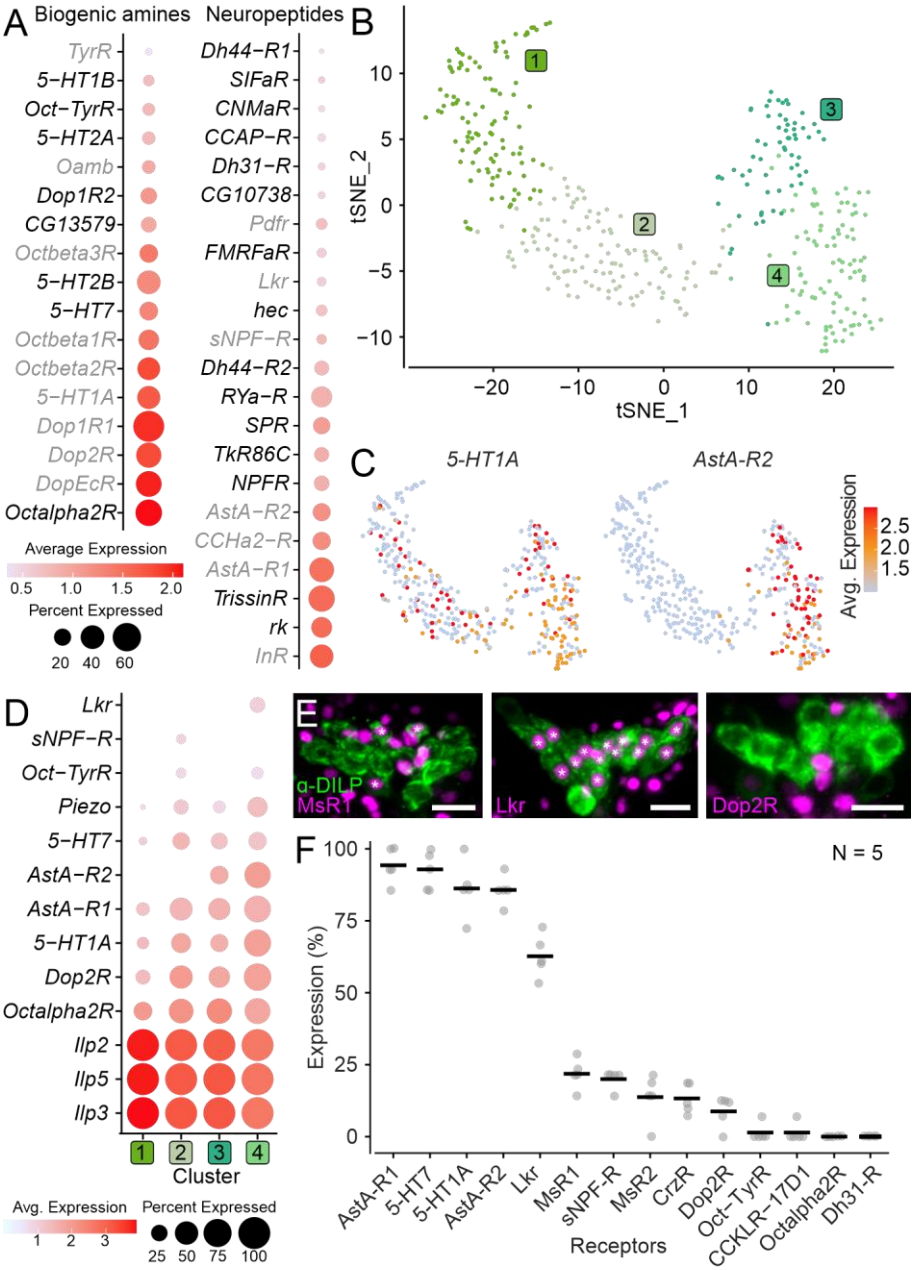

Figure 1: Expression of neuromodulator receptors in IPCs. A: Expression of biogenic amine and neuropeptide receptors in IPC single-nucleus transcriptomes. Novel receptors are depicted in black, and receptors previously shown to be expressed in IPCs are shown in gray. **B**: t-SNE plot based on unsupervised clustering of IPC transcriptomes reveals 4 clusters. **C:** t-SNE plots showing expression of 5-HT1A receptor and Allatostatin-A receptor 2. **D**: Expression of IPC markers (*Ilp2*, *Ilp3*, *Ilp5* and *Piezo*) and select neuromodulatory receptors across different IPC clusters. Note that some receptors are expressed in all clusters while others are only expressed in a subset of clusters. **E:** Maximum projection of representative confocal images showing receptor-T2A-GAL4 driven mCherry expression (magenta) in IPCs (labelled using DILP2 antibody in green). Asterisks indicate IPCs whose nuclei are stained. Scale bars = 10 µm. **F:** Fraction of IPCs expressing select receptors based on T2A-GAL4 driven mCherry expression in IPCs. Averages are based on 5 preparations for each receptor. See Table S1 for all abbreviations.

IPCs are heterogeneous in their receptor expression profiles

IPCs have generally been regarded as a homogeneous population of approximately 14 cells that can be anatomically identified using antibodies against DILP2, 3 or 5. However, recent evidence suggests that IPCs can be separated into at least two subgroups based on the expression of the mechanosensitive channel Piezo in only a subset of IPCs (Wang et al., 2020). Moreover, previous studies also revealed a division of the IPCs in subgroups based on heterogeneous responses to clock-neuron stimulation and to glucose (Oh et al., 2019; Barber et al., 2021). Our analysis also indicated that *Piezo* is only expressed in a subset of IPCs (Figure S1A). Hence, we probed further to see if the receptors expressed in IPCs (Figure 1A) were differentially expressed across IPCs, lending further support for the heterogeneity of the IPC population. For this, we performed unsupervised clustering of all IPC transcriptomes based on highly variable genes and visualized it using t-SNE analysis (Figure 1B). This analysis retrieved four clusters that were not very distinct, suggesting a lack of drastic variability in gene expression across individual IPCs. Nonetheless, examining the expression of 10 neuromodulator receptors that were selected to represent neuropeptides and amines, as well as low and high receptor expression, revealed cluster-specific differences (Figure 1C & D and S2). For instance, *5-HT1A* was expressed in all four clusters, *AstA-R2* was expressed in two clusters (Figure 1C & D), while *short neuropeptide F receptor* (*sNPF-R*) was only expressed in one cluster (Figure 1D and S2). Other receptor genes, such as *Piezo*, were expressed across all clusters but at drastically different levels and in different fractions of IPCs. Hence, differences in receptor expression profiles, based on transcriptome sequencing, support the conclusion that the IPCs are a heterogeneous population.

Anatomical mapping of neuromodulator receptors complements single-nucleus transcriptome profiling of IPCs

Single-nucleus transcriptomes can prove extremely powerful in examining global gene expression differences at a cellular resolution. However, it has limitations, including contamination by ambient RNA, which can give rise to false positives (Allen et al., 2020). To assess the reliability of our expression analysis, we verified the expression of 14 neuromodulator receptors in IPCs, using anatomical techniques. We primarily used T2A-GAL4 knock-in lines (Deng et al., 2019; Kondo et al., 2020) to drive expression of nuclear mCherry under the control of endogenous neuromodulator receptor promoters and then quantified the percentage of IPCs expressing mCherry for each receptor line using immunohistochemistry (Figure 1E, 1F and S3-S5). In accordance with previous anatomical investigations (Kapan et al., 2012; Luo et al., 2012; Hentze et al., 2015; Zandawala et al., 2018; Yurgel et al., 2019) and our transcriptome analysis, receptors for AstA, LK, sNPF, and 5-HT were all expressed in the IPCs (Figure 1E & F, S3 and S4). Importantly, the expression of several novel neuromodulator receptors that we identified by our sequencing analysis was confirmed as well. For instance, all five serotonin receptor transcripts were detected in the IPC transcriptomes, one of which (*5-HT7*) was further confirmed

using anatomical mapping (Figure 1A, 1F, S3 and S4). These receptor mapping experiments also indicated that not all IPCs are identical as some receptors were expressed in only a subset of IPCs (Figure 1F and S4). For example, AstA-R2 was expressed in 86%, Lkr in 63%, and sNPF-R and myosuppressin (MS) receptor 1 (MsR1) in about 20% of IPCs. Thus, each receptor type is expressed by a different fraction of IPCs, implying that IPCs consist of more than two subgroups. Across individuals, however, the fractions of IPCs expressing a given receptor were consistent, suggesting that receptor expression is tightly regulated (Figure 1F). We used percent expression similar and lower than corazonin receptor (CrzR) (Figure 1F) as threshold to determine a receptor as not expressed in IPCs based on anatomical mapping (Figure S5). This was justified based on the fact that the average CrzR expression (13.3%) was lower than one pair of IPCs (2 out of 14 or 14.3%) per brain, and previous studies reported a lack of CrzR expression in IPCs (Oh et al., 2019; Zandawala et al., 2021). Our anatomical mapping largely correlated with our single-nucleus sequencing analysis. Exceptions to this included the two MS receptors, MsR1 and MsR2. T2A-GAL4 lines for both receptors drove expression in a small subset of IPCs but the expression of their transcripts in the IPC transcriptomes was below the 5% threshold used here (Figure 1D-F, S3 and S4). Hence, neuromodulator receptors with low expression levels could be expressed in the IPCs in addition to the ones reported here based on the single-nucleus transcriptomic analysis. Other differences between the gene expression analysis and anatomical mapping were exemplified by the dopamine receptor *Dop2R* and the octopamine receptor *Octα2R*, which were both highly expressed in the IPC transcriptomes but were not detected using anatomical mapping (Figure 1A, 1F and S5). To determine if these discrepancies were due to the presence of additional receptor transcript variants with different C-termini that may not be under the control of the T2A-GAL4 knock-in lines, we utilized a Trojan-GAL4 which should represent expression of other *Octα2R* transcript variants. Surprisingly, this general GAL4 line for *Octa2R* also did not drive expression in IPCs (Figure S5). Given that G-protein coupled receptors (GPCRs) are usually expressed in low amounts, it is highly unlikely that these receptors represent false positives due to ambient RNA contamination during sample preparation for transcriptome sequencing (Sriram et al., 2019). Hence, inadequate transgenes are the likely cause for the discrepancy between transcriptome analysis and anatomical mapping.

In summary, anatomical receptor mapping complemented the single-nucleus transcriptome analysis and confirmed the heterogeneous expression of several novel neuromodulator receptors in IPCs. Using two different methods to assess expression of receptors in IPCs also demonstrated the necessity of parallel approaches to obtain accurate insights into receptor expression in complex modulatory systems.

IPC activity is modulated by aminergic and peptidergic neurons

Previous studies and our receptor expression data suggested that the IPC activity could be modulated by several different modulatory systems acting in parallel, which could ultimately affect insulin release. However, the functional significance of these pathways remains unknown. Therefore, we next sought to investigate how the activation of specific modulatory populations, leading to the intrinsic release of neuromodulators, affects IPC activity *in vivo*. For this, we recorded the activity of individual IPCs via whole cell patch-clamp while optogenetically activating different populations of modulatory neurons via the cationic channelrhodopsin CsChrimson (Figure 2A & B). We used nine different driver lines targeting different populations of modulatory neurons (MNs) for the activation experiments. Receptors for most of the neuromodulators found in these neurons were expressed in IPCs according to our expression analyses. We further included a driver line for neurons expressing adipokinetic hormone (AKH), since it was previously shown to influence DILP3 release in larvae (Kim & Neufeld, 2015). Hence, all nine of these MNs have been suggested to affect IPC activity or play a role in metabolic homeostasis and feeding (Birse et al., 2011; Luo et al., 2014; Hallier et al., 2016; Nässel & Vanden Broeck, 2016; Gough et al., 2017; Takeda et al., 2018; Zandawala et al., 2018; Nässel & Zandawala, 2019; Oh et al., 2019; Yurgel et al., 2019; Nässel & Zandawala, 2020; Lin et al., 2022). These specific MN driver lines targeted neurons containing the biogenic amines dopamine (DANs), octopamine (OANs), or serotonin (5-HTNs), as well as the neuropeptides AstA (AstANs), AKH (AKHNs), diuretic hormone 31 (DH31Ns), LK (LKNs), MS (MSNs), or tachykinin (TKNs, Figure S6). We also included a line that we expected to target sNPF-expressing neurons, but anatomical labeling revealed later that the line was in fact empty and, therefore, lent itself as control line (Figure S6, S7B and S7C). While some of these modulators are expressed and released by large populations of neurons forming distinct subpopulations (e.g., AstA, DA, and 5-HT), others are expressed in very few individually identifiable neurons (e.g., LK and AKH). Accordingly, the number of targeted neurons varied between driver lines (Figure S6). During these intrinsic pharmacology experiments, we first recorded the baseline activity of IPCs, which had a membrane potential of about -40 mV without subtraction of the 13mV liquid junction potential (Gouwens & Wilson, 2009). The spike frequency was 0.8 Hz on average, in flies fed ad libitum. Activating individual MN populations showed strong and immediate effects on IPC activity in several cases (Figure 2C). In order to classify IPC responses using a data-driven approach, we implemented threshold criteria for the membrane potential to cluster the IPCs depending on the effects of MN activation into excited, inhibited, or unaffected (Figure 2C, for details see Material and Methods). Excitation was characterized by a fast depolarization of the membrane potential, often accompanied by an increase in spike frequency shortly after the onset of activation (Figure 2C, magenta). Opposite to this, inhibition was characterized by a hyperpolarization of the membrane potential and a reduction in spike frequency (Figure 2C, blue). Unaffected IPCs showed no significant changes after activation compared to the baseline (Figure 2C, black). For each recorded IPC, we activated the MNs repeatedly for ten trials. Individual IPCs showed consistent responses to repeated activation (Figure 2C and S7A). Using this approach, we quantified and categorized the effect of each MN population on the IPC activity.

First, we quantified the global effect of each MN population on the IPC population activity. To this end, we calculated a general effect coefficient that was based on the mean area under the curve (AUC) of the membrane potential of all recorded IPCs after MN activation (see Material and Methods for calculation details), describing a global trend for the shift in IPC activity (Figure 2D). This coefficient was highest for DAN activation (0.51), meaning the overall activity of the IPCs was strongly shifted towards excitation. OAN activation also led to

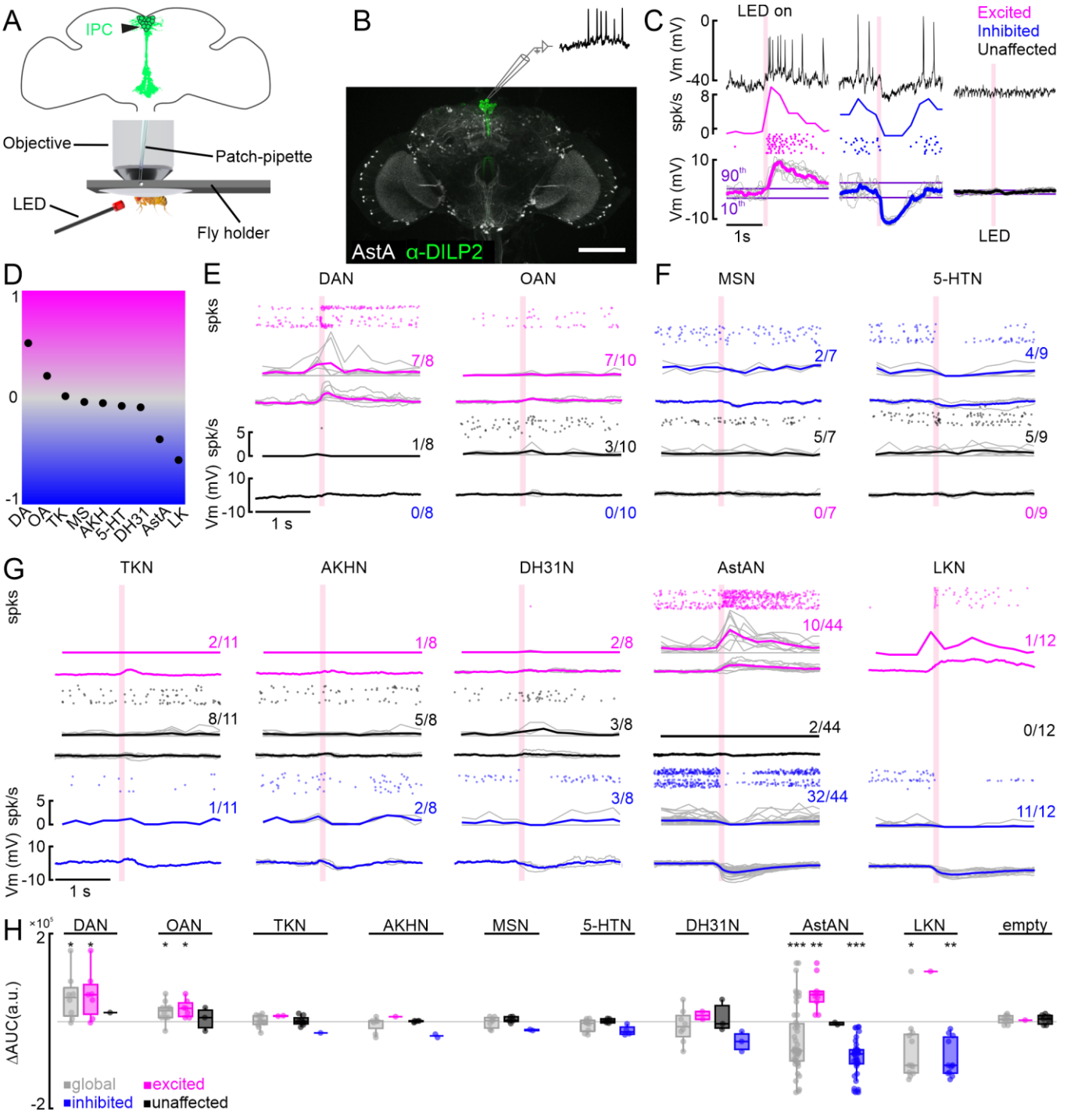

Figure 2: Modulation of individual IPCs by aminergic and peptidergic neurons in patch-clamp recordings. A: Schematic of setup for patch-clamp recordings and optogenetic activation. **B:** Anatomy of example driver line labeling AstANs (gray) and antibody staining against DILP2 labeling IPCs (green). **C:** Example responses of three IPCs to optogenetic activation of AstANs (red bar). IPCs with a membrane potential (Vm) rising above the 90th percentile of the baseline during or after stimulation were defined as "excited" (magenta). IPCs with Vm falling below the 10th percentile were defined as "inhibited" (blue). IPCs remaining between the thresholds were "unaffected" (black). **D:** Normalized overall trends across all tested lines based on the area under the curve (AUC) average of all recorded cells for the respective line. **E:** DAN, and OAN populations primarily drove excitation or had no effect on IPCs upon activation. Spike events (dots), spike frequency (spk/s), and low-pass filtered Vm (mV) are shown, color-coded according to the clusters as before. Gray lines indicate individual IPCs, while color-coded lines show the cluster average. Fractions indicate number of IPCs per cluster. **F:** MS- and 5-HT-expressing neurons had inhibitory or no effects on IPCs. Details as in D. **G:** TKNs, AKHNs, DH31Ns, AstANs, and LKNs evoked mixed effects in IPCs upon activation. Details as in D. **H:** Baseline subtracted AUC values (ΔAUC) of all recorded cells (gray), and excited (magenta), unaffected (black), and inhibited (blue) clusters. P-values were calculated using the Wilcoxon signed-rank test.

a positive coefficient (0.2), indicating a weaker excitatory shift. Activation of TKNs (0.01) and MSNs (-0.04) both resulted in a coefficient near zero and therefore did not shift the overall activity. AKHNs (-0.05), 5-HTNs (-0.08), and DH31Ns (-0.09) shifted the activity of the IPC activity slightly towards inhibition. Activating AstANs (-0.39) had a stronger inhibitory effect, and the activation of LKNs (-0.58) led to the strongest inhibition of IPCs.

Next, we analyzed the effects of each MN population had on individual IPCs in more detail. Activation of DANs and OANs either excited or had no effect on individual IPCs (Figure 2E). DAN activation resulted in a strong excitation in the

majority of IPCs (7/8), and only 1/8 IPCs remained unaffected. Activation of OANs also strongly excited most IPCs (7/10), while 3/10 IPCs showed no effect (Figure 2E). In contrast, activation of MSNs and 5-HTNs, either inhibited or had no effect on individual IPCs (Figure 2F). However, in one IPC, there was reliably a single spike upon activation of 5-HTNs but the average membrane potential did not meet our threshold and therefore it was not labeled excited. Activation of MSNs led to the inhibition of 2/7 IPCs, while 5/7 remained unaffected. Activating 5-HTNs inhibited 4/9 IPCs and had no effect on 5/9 (Figure 2F). Surprisingly, activating neuronal populations expressing AstANs, AKHNs, DH31Ns, LKNs, or TKNs, had different effects on different subsets of IPCs. Here, we found IPCs exhibiting all three response types (excited, inhibited, and unaffected) during activation of the same MNs (Figure 2G). When activating TKNs, the IPC response was distributed in 2/11 excited IPCs, 1/11 inhibited, and the majority with 8/11 remained unaffected. With the activation of AKHNs, only 1/8 IPCs was excited and 2/8 inhibited, while 5/8 remained unaffected. Activating DH31Ns had a stronger effect than AKHNs, with 2/8 excited IPCs, 3/8 inhibited, and only 3/8 remained unaffected. Interestingly, AstAN activation resulted in strong excitation and inhibition. Hence, we decided to analyze the effects of AstANs on IPCs in more detail by increasing the sample size. We found that 10/44 recorded IPCs were excited upon activation, while the largest subset with 32/44 were inhibited, and only 2/44 remained unaffected. LKNs showed an even stronger inhibitory effect, since the activation led to only 1/12 excited IPCs, while 11/12 were inhibited. We also recorded from IPCs while activating the line that was expected to express CsChrimson in sNPFNs but was in fact empty (Figure S6 and 7D). Accordingly, "activating" this line while recording from IPCs had no effect on the IPC activity, except for one cell where the membrane potential increased slightly (Figure S7D).

To analyze the effect strength for all lines, we subtracted the baseline AUC, calculated before the activation onset, from the AUC after activation (ΔAUC). To determine if the effects were significant for the respective line, we calculated the p-values using the Wilcoxon signed-rank test for all recorded IPCs and for individual clusters with a minimum number of 5 recorded IPCs. Our analysis revealed that only the effects of DANs, OANs, AstANs, and LKNs were significant (Figure 2H). For DANs and OANs, we found a significant effect for the population of all recorded IPCs and in the excited cluster. For LKNs, on the other hand, the IPC population and the inhibited cluster showed a significant effect. AstAN activation led to a significant effect in the IPC population, the excited and the inhibited cluster. TKNs, AKHNs, MSNs, 5-HTNs, and DH31Ns also had effects on the IPC activity, especially in the clusters we found for the respective line, but they were not statistically significant.

Taken together, these results show that different populations of MNs have distinct effects on the IPC activity. The heterogeneous effects the activation of individual MN populations had on IPCs could arise from the heterogeneous receptor profiles exhibited by individual neurons in the IPC population. In addition, our intrinsic pharmacology approach targets not only the respective neuromodulator release but activates the whole neurons leading to a broad release of modulators and transmitters. Therefore, IPC responses could be driven both by the respective neuromodulator and by the co-release of classical, fast-acting neurotransmitters possibly present in those neurons. This co-transmitter release occurs under naturalistic circumstances (Croset et al., 2018), and our IPC transcriptome analysis showed that IPCs express receptors for the classical transmitters ACh, Glu, and GABA (Figure S1).

The high temporal resolution of our *in vivo* patch-clamp recordings enabled us to analyze the detailed temporal dynamics of IPC modulation. Here, we focused on DANs, OANs, AstANs and LKNs, which had strong, significant effects on the IPC activity (Figure 2H). We quantified the latency from activation onset to IPC de- or hyperpolarization for each MN population (Figure 3A). All MNs had rapid effects on the IPC activity, with DANs driving the fastest excitatory effects at a median latency of 10 ms, while OANs had the slowest with a median latency of 122 ms. The inhibitory effect of AstAN and LKN activation occurred with a similar median latency of 49 ms and 43 ms, respectively.

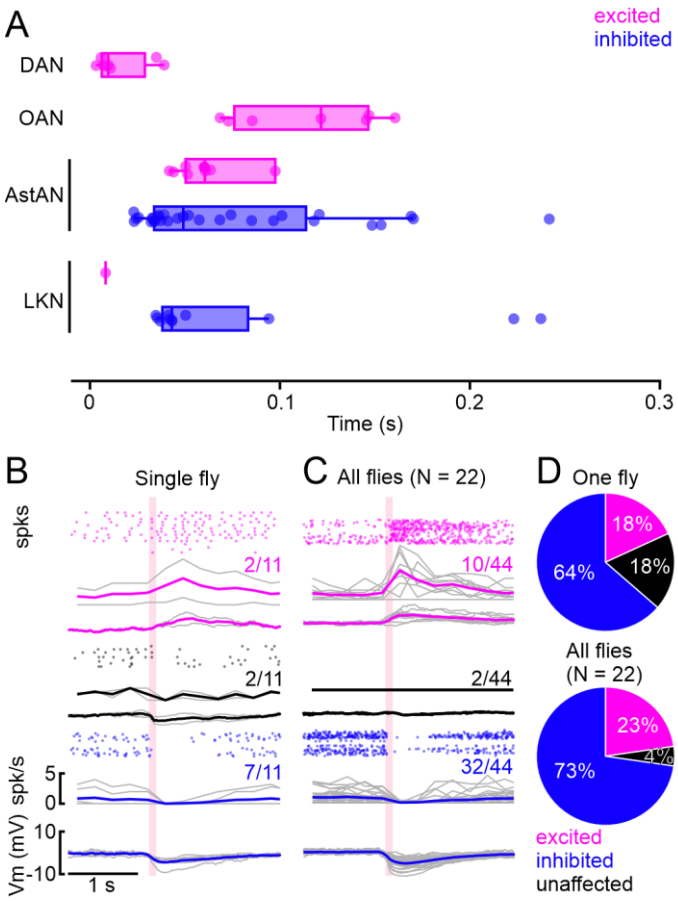

Figure 3: Latency analysis and singly fly recordings. A: Threshold-based latency analysis for excited (magenta) and inhibited (blue) IPCs during activation of DANs, OANs, AstANs, and LKNs, which had significant effects on the IPC activity upon activation. Activation onset at 0 s. Boxplots show median and interquartile range, dots represent individual recordings. Three outliers for AstAN between 0.4 and 0.8 not shown for clarity of inspection. **B:** Patch-clamp recordings of 11 IPCs subsequently patched in the same fly reveal a similar distribution of excited, inhibited, and unaffected IPCs compared to the distribution of IPCs recorded across all flies (C). **C**: All recordings across 22 flies upon AstAN activation. Plot from Figure 2G. **D:** Cluster distribution across 11 cells in one fly and in 44 cells in 22 flies.

Classical monosynaptic connections have a response latency of a few milliseconds (Griffith, 2012), which is much faster than the latencies we observed. We therefore assume that the majority of the effects we observed were not due to direct, monosynaptic input to the IPCs. Instead, they are likely driven

by polysynaptic or modulatory connections. Only the excitatory effects of DANs and the single excited IPC during LKN activation were on a timescale that could indicate monosynaptic connections.

Heterogeneous IPC responses occur within the same animal

The heterogeneity we observed in the functional connectivity between MNs and individual IPCs during patch-clamp recordings could have three different origins: 1) It could reflect differences in synaptic connectivity between different animals. 2) Functional connectivity between MN populations and IPCs could change over time. For example, the heterogeneity could arise from changes in the animal's internal state, including starvation or changes in behavior, such as increased leg-flailing, which readily occurs during *in vivo* recordings. We controlled for some, but not all these aspects, for example by providing food to all animals ad libitum until we prepared them for experiments and by continuously perfusing the brain with the same, sugar-containing saline. 3) The heterogeneity could be a persistent feature of IPC modulation, allowing for a more nuanced shift of IPC population activity through the action of modulatory neurons on individual IPCs. This nuanced modulation would be beneficial considering that insulin release is critical for metabolic homeostasis and needs to be flexibly adjusted to various contexts with a relatively small population of IPCs.

To determine if the heterogeneity was a result of inter-individual differences in connectivity and/or internal states, we tested whether IPC response patterns were less heterogeneous when recording from multiple IPCs in a single animal, rather than inferring the population activity from individual recordings across animals. We therefore subsequently recorded from 11 IPCs in the same fly while activating AstANs. Remarkably, responses across the population of IPCs recorded successively in the same fly were just as heterogeneous as responses recorded across flies: 2/11 IPCs were excited, 7/11 inhibited, and 2/11 remained unaffected in the same fly (Figure 3B & D). These heterogeneous responses and their distribution in a single animal mirrored the responses of IPCs recorded across multiple animals (Figure 3C & D). Recording the activity of multiple IPCs in four additional animals showed similar heterogeneous response profiles (Figure S8). Hence, heterogeneous IPC responses are not accounted for by inter-individual differences. Instead, the heterogeneity occurred within single animals and appears to be a persistent feature of IPC modulation.

Heterogeneous responses of individual IPCs underlie shifts in population activity

Our recordings from multiple IPCs in the same animal revealed that the heterogeneous responses are not based on functional differences between individuals. In principle, however, the heterogeneity could still arise from changes in connectivity over time, for example due to internal state changes, since we only recorded one IPC at a time in our patch-clamp experiments. Therefore, we next recorded from multiple IPCs simultaneously via *in vivo* widefield calcium imaging, to address whether excitatory and inhibitory responses were elicited at the same time in the same animal and to gain an understanding of the IPC population dynamics (Figure 4A). To this end, we recorded the calcium dynamics in IPCs during the activation of DANs, OANs, or MSNs. We chose these lines since they generated the full spectrum of responses from primarily excitatory to inhibitory in patch-clamp recordings. In addition, we selected lines targeting AstANs and LKNs, which elicited heterogeneous effects in our patch-clamp recordings. We tested different activation durations to account for the slower dynamics of the calcium indicator (Figure S9A). A 5 s long activation seemed most appropriate, since it elicited consistent IPC responses while ensuring that IPCs retained naturalistic activity patterns throughout the duration of the experiment (Figure 4A-C, and S9B).

Activation of the selected driver lines evoked strong and immediate fluorescence changes across the IPC population (Figure 4 C). When comparing IPC responses during two consecutive activations, we found that the same subset of IPCs showed a fluorescence increase during both activations while other IPCs consistently showed a decrease (Figure 4D). Hence, individual IPC responses were consistent across trials, just like in our electrophysiology experiments. Therefore, we performed a threshold-based analysis to cluster the responses of individual IPCs into excited, inhibited, and unaffected, analogously to the approach used for electrophysiology data (Figure 4E, see for details Material and Methods). Imaging multiple IPCs simultaneously revealed that the three activity clusters occurred within the same animal, and at the same time (Figure 4E). We visualized the $\Delta F/F$ traces for each recorded IPC for all animals in the respective MN line as heatmaps (Figure 4F). These high-resolution heatmaps depict the effects of the respective MN activation on all recorded IPCs, across all animals. For example, the activation of AstANs led to a fluorescence increase in the majority of IPCs across all animals, while the activation of MSNs decreased the fluorescence in most IPCs in all tested animals (Figure 4F). However, we also found differences between individual animals. For example, during the activation of OANs, IPCs in flies #2, 5, and 6 were primarily excited, while IPCs in fly #4 were primarily inhibited. Interestingly, we found heterogeneous IPC responses across all driver lines, independent of the strength or valence of the global trend of the IPC population (Figure 4F). Recording from multiple IPCs at the same time uncovered that within one cluster, the response seemed homogeneous, e.g., in fly #4 during the activation of DANs (Figure 4F).

The threshold-based cluster analysis revealed three clusters based on the responses of the IPCs to the activation of the respective driver line for all MNs tested (Figure 4G). To further quantify the effects of MNs on IPCs and to assess whether they were statistically significant, we compared the activity of each IPC before activation to the activity after activation based on the AUC of individual $\Delta F/F$ traces (Figure 4H). First, we performed this analysis across the entire IPC population for each driver line. Second, we analyzed the IPCs by cluster, i.e., the excited, inhibited, and unaffected IPCs separately. AstANs, OANs, and DANs had significant overall effects on the population activity, driving a net increase in IPC activity (Figure 4H, gray). For these MNs, the effects were also significant when considering the inhibited and excited cluster separately (Figure 4H, blue and magenta). MSN activation significantly inhibited the IPC population activity, an effect that was carried solely by a significant effect on the inhibited IPC cluster (Figure 4H, blue). LKN activation had significant effects in the excited and inhibited clusters, but those canceled each other out in the pooled data, resulting in no net excitation or inhibition (Figure 4H, gray). The global effect of each MN population on the IPCs is summarized in Figure 4I. This analysis demonstrated the effect strength during the activation of the respective MNs and their state, while MSNs shifted the population activity towards inhibition (Figure 4I).

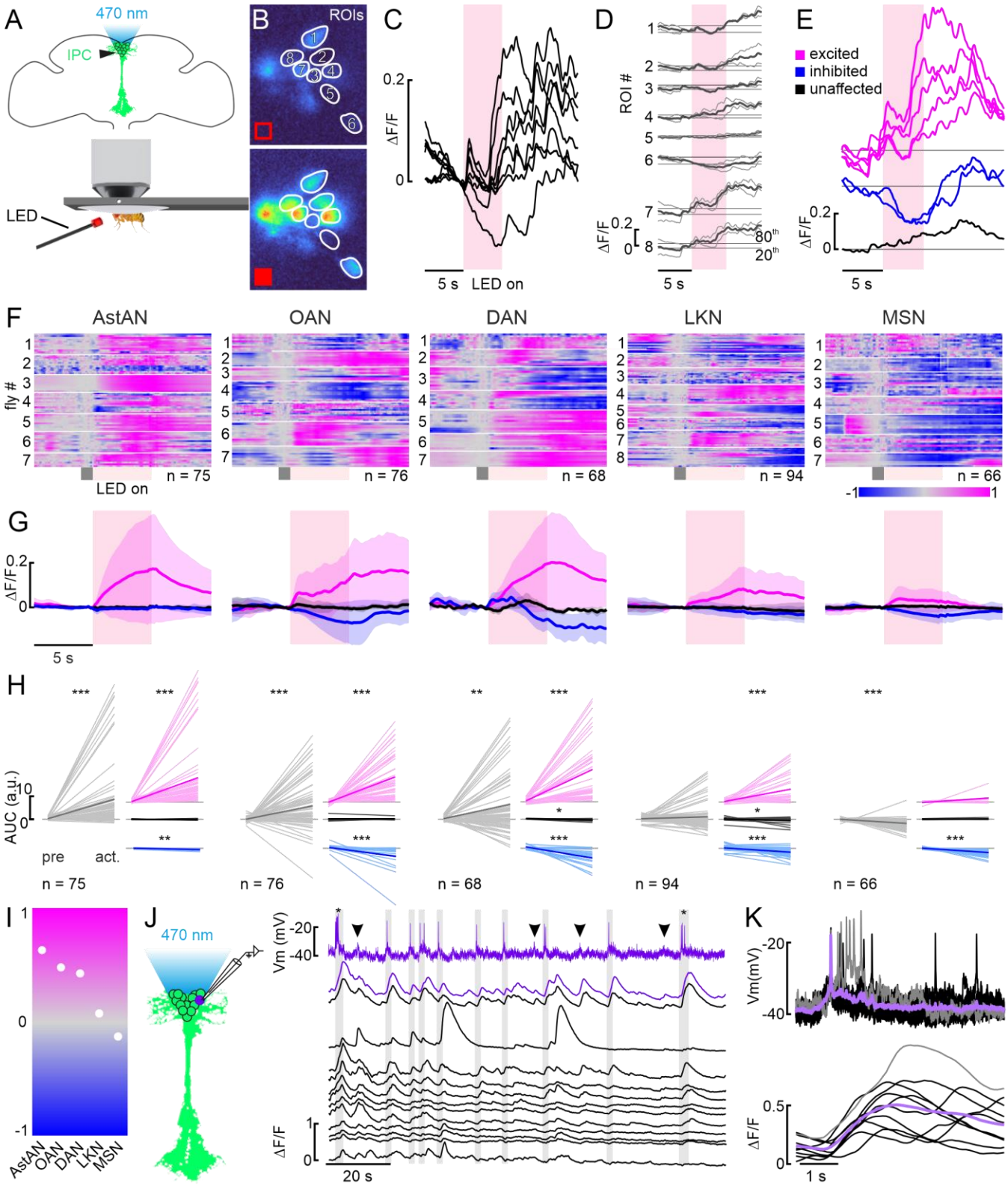

Figure 4: Modulation of the IPC population by aminergic and peptidergic neurons in calcium imaging experiments. A: Schematic of the setup for optogenetic activation during calcium imaging. **B:** example images of the GCaMP6m-expressing IPC cell bodies, delimited as ROIs during a time series before and during a 5 s optogenetic activation of OANs **C:** Normalized ΔF/F traces for ROIs in B during one activation (red shading). **D:** Superimposition of two subsequent activations (thin lines) and the mean of both (thick line) that was used for further analysis steps. **E:** Cluster analysis based on the 20th and 80th percentile of the baseline (see Material and Methods) revealed three cluster within this one example animal. **F:** Heatmaps of the mean ΔF/F traces of all recorded IPCs per driver line. Traces were baseline subtracted based on the activity during a 1 s window (gray box) before the 5 s activation (red box). **G:** Mean ΔF/F traces (thick lines) for each cluster (color-coded as before) with respective standard deviation (shaded areas). Data correspond to the respective driver line indicated in F.**H:** AUC of IPCs before activation (pre) and during activation (act.; from onset to 5 s after activation) for all recorded IPCs (grey, left) and for the three clusters (colors, right). P-values were calculated using the Wilcoxon signed-rank test (see Table 4 for all p-values). **I:** Overall trends across all tested lines based on the AUC averaged across all IPC responses. **J:** Simultaneous recording of one IPC via patch-clamp (first row, purple Vm trace), and the same IPC (second row, purple ΔF/F trace) as well as 12 additional IPCs (black ΔF/F traces) via calcium imaging. **K:** Superimposition of action potentials from J and corresponding ΔF/F trace (black traces, individual events, lavender trace, mean, gray trace shows burst of spikes and respective ΔF/F trace).

In addition to the population-level analysis, calcium imaging allows the investigation of receptor-dependent calcium dynamics that are not coupled to electrical activity. For example, intracellular calcium mediates gene expression in addition to neuronal signaling (Venkiteswaran & Hasan, 2009; Brini et al., 2014), which might underly long-term changes in IPC activity. Our intrinsic pharmacology experiments during calcium imaging revealed that activating AstANs and LKNs caused calcium dynamics that were not necessarily predicted from electrophysiological data. For example, in both cases, we observed strong increases in calcium in the IPCs, which occurred in addition to the inhibition recorded via patch-clamp. Especially AstAN activation resulted in a fast and robust calcium influx across the majority of recorded IPCs. This calcium increase could lead to an increase in insulin release, but also to alterations in gene transcription, for example.

To investigate how the electrophysiological activity recorded in patch-clamp translates into calcium signals in IPCs, we recorded the spontaneous baseline activity from one IPC via patch-clamp while performing calcium imaging of 13 IPC cell bodies (ROIs) without activating any MNs. When comparing the membrane potential with the fluorescence traces of the same IPC, it became evident that fluorescence increases matched the occurrence of action potentials faithfully (Figure 4J, gray boxes and purple traces), as indicated before for IPCs (Liessem et al., 2023). Accordingly, a burst of action potentials led to a prolonged and stronger calcium influx (Figure 4J asterisks). By superimposing the action potentials and the associated fluorescence traces, the close correlation became even more apparent (Figure 4K), with the expected delay for calcium imaging rooted in the kinetics of GCaMP6m (Chen et al., 2013). However, when inspecting the membrane potential and the fluorescence trace of the patched IPC more closely, we noticed that in some instances calcium influxes were not driven by action potentials, but by subthreshold depolarizations (Figure 4J, arrowheads). Hence, while there was a strong correlation between IPC spiking and calcium influx, calcium dynamics were not solely coupled directly to membrane potential changes.

Interestingly, when comparing the fluorescence traces of all 13 IPCs with each other, we found that the fluorescence dynamics were synchronized between some, but not all IPCs (Figure 4J). This suggests that some IPCs either receive the same input or form reciprocal connections, while others receive different inputs and are not coupled to the same sub-population. This further demonstrates that IPCs form distinct clusters.

Taken together, our intrinsic pharmacology experiments using calcium imaging showed that the different modulatory populations had immediate effects on the IPC activity.

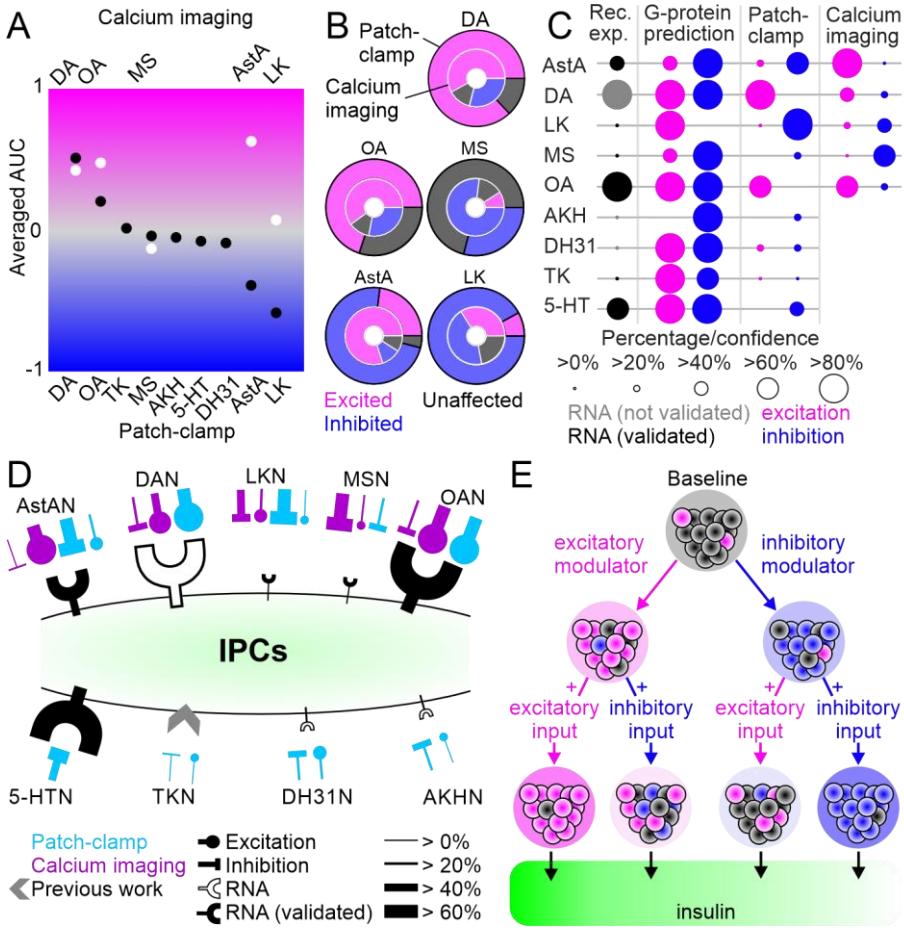

Figure 5: Summary of neuromodulation of IPCs. A: Comparison of overall activity shifts for all driver lines and IPCs tested between patch-clamp (black) and calcium imaging (white). **B:** Comparison of cluster proportions between patch-clamp (outer circles) and calcium imaging (inner circles). **C:** Comparison of, expression data, G-protein coupling prediction, patch-clamp recording, and calcium imaging. Dots indicate percentage of IPCs for expression data, patch-clamp, and calcium imaging, and the confidence for G-protein prediction. For receptor expression data, black dots indicate the expression has been validated with receptor mapping. **D:** Simplified model of IPC modulation. Overview of receptor expression and functional connectivity in patch-clamp (blue) and calcium imaging (purple) recordings for all modulatory inputs tested. Line thickness indicates fraction of involved IPCs. Receptor expression for TK from (Birse et al., 2011). **E:** Simplified hypothesis of IPC population activity shifts through excitatory or inhibitory modulator input and the effects of consecutive input on insulin output.

The overall trends of the IPC population activity ranged from a strong calcium increase during the activation of AstANs to mostly inhibited during the activation of MSNs (Figure 5A). For DANs, OANs, and MSNs the activation led to comparable global shifts in the population activity between calcium imaging and patch-clamp. DANs and OANs had a strong excitatory effect, while MSNs had a slightly inhibitory effect. For AstANs and LKNs, calcium imaging revealed additional activity dynamics compared to patch-clamp recordings. In patch-clamp recordings, AstANs elicited a strong inhibitory effect on the majority of IPCs and a strong excitation in a smaller subset. In calcium imaging, AstAN activation led to a strong calcium increase in the majority of IPCs. LKN activation also had a stronger inhibitory effect in patch-clamp recordings compared to calcium imaging experiments, which is apparent when comparing the global trends of both lines between methods (Figure 5A). Those similarities and differences in the overall effect were not only driven by the effect strength, but also by the number of affected IPCs. For DAN, OAN, and MSN activation, the number of cells per cluster was similar in patch-clamp and imaging, while for AstANs, and LKNs the affected fraction of

IPCs per cluster differed considerably (Figure 5B). On a single cell level, we found heterogeneous responses while imaging multiple cells at the same time during activation of the same MN population. This is a strong indicator that the response clusters we saw in patch-clamp recordings are not due to state-dependent shifts between recordings. Instead, the simultaneous calcium imaging recordings indicated that the heterogeneous responses are a persistent feature of the IPC population. Within any given cluster, the responses appeared highly homogeneous, indicating that within one response cluster the modulatory input to the associated IPCs was similar.

To link our receptor expression analyses with the valence of the connectivity observed in electrophysiological recordings and calcium imaging, we analyzed the G-protein coupling scores for all the receptors of interest, including multiple splice isoforms where relevant (see Table S2 for details; http://athina.biol.uoa.gr/bioinformatics/PRED-COUPLE2/). To simplify comparisons, we predicted that a neuromodulator could be excitatory if at least one of its receptors (including transcript variants) coupled to Gs or Gq proteins. Similarly, a neuromodulator was predicted to be inhibitory if at least one of its receptor variants was predicted to couple with Gi protein. When comparing the predictions and anatomical mapping results with the results from patch-clamp recordings and calcium imaging, it became apparent that the majority of MN activation effects were correctly predicted by the receptor profile (Figure 5C). For example, AstA receptors were predicted to signal via both excitatory and inhibitory secondary messenger pathways, which could explain the heterogeneity and the differences observed between patch-clamp experiments and calcium imaging. On the other hand, we expected that LKN activation would primarily result in IPC excitation, but this contrasts with our patch-clamp and calcium imaging experiments. Hence, the effects of LKN activation on IPCs are likely due to other factors, e.g., indirect connections between LKNs and IPCs, and potentially other neurotransmitters co-released by LKNs upon activation. However, for the majority of investigated MNs, their global effect on the IPC activity can be predicted based on receptor expression and G-protein coupling, which can also account for the heterogeneous effects.

Discussion

Our results show that the activity of IPCs in *Drosophila* is affected by multiple neuromodulatory inputs. We unraveled the receptor profile of IPCs and the effects of nine key MN populations on the IPCs on the level of single-cell responses and population activity shifts (Figure 5C and 5D). Hence, our study provides a multi-level quantification of the complex regulation of IPCs which underlies their ability to respond to ever-changing metabolic demands and environmental inputs.

General effects on the IPC activity

Neuromodulation enables multiplexing in neuronal circuits and lends flexibility to seemingly hard-wired connections. In contrast to classical, fast-acting neurotransmitters, neuromodulators can act far away from their release sites, and thus change neuronal circuit dynamics across the entire nervous system. Due to the complexity of neuromodulatory systems, studies examining their functions or modes of action have often been limited to *ex vivo* preparations or *in vitro* physiological assays (Bargmann & Marder, 2013). Here, we leveraged the IPCs of *Drosophila* as a model system to investigate neuromodulation by combining multiple approaches, including *in vivo* patch-clamp recordings and calcium imaging, as well as receptor expression mapping. Our results revealed that the IPC population activity can be shifted towards excited or inhibited states on fast timescales through the action of different MN populations. Hence, some MNs have strong, immediate effects on the global IPC activity, which could prime the system for pending metabolic demands by altering the excitability of IPCs and ultimately affect insulin release. Furthermore, prolonged activation protocols during patch-clamp recordings and calcium imaging experiments demonstrated that these effects persist during continued activation (Figure S7A & B and S9A). This indicates that the input of the respective MNs could also affect the IPC activity on longer timescales. These effects on long timescales could in turn affect the IPCs on two levels: 1) sustained excitation could lead to a direct increase in insulin release and 2) continuous activation of IPCs through modulatory inputs could also lead to altered gene expression, e.g., resulting in increased expression of *ilp*(*s*) (Li & Gong, 2015; X. Chen et al., 2016). Prolonged inhibition could have the opposite effects, with a decrease of insulin release and ultimately a decrease in *ilp* expression.

Although most MNs investigated in our study co-express other neuronal signaling molecules, e.g., additional neuropeptides and fast-acting neurotransmitters (Croset et al., 2018), we focus on functions of the neuromodulators that define the populations, especially in relation to insulin signaling. For example, activating DANs and OANs shifted the IPC population activity towards an excited state in patch-clamp recordings and calcium imaging. In *Drosophila*, DA is implicated in modulating locomotion, learning, and courtship behavior (Yamamoto & Seto, 2014; Siju et al., 2021). In female flies, DA directly acts on the IPCs via DopR1, which affects ovarian dormancy via effects on DILP signaling (Andreatta et al., 2018). Our results demonstrate that DANs have a fast and strong excitatory effect on the IPC activity *in vivo*, on short time scales. However, ovarian dormancy is accompanied by diminished insulin signaling and is likely controlled over longer time scales. Hence, there might be an additional long-term effect of dopamine on IPCs, which we have not explored here.

Our finding that OANs had strong, fast, excitatory effects on IPCs in patch-clamp recordings and calcium imaging, was somewhat unexpected. This is because the actions of OA are antagonistic to those of insulin in several contexts. For example, OA drives increases in locomotor activity and foraging behavior while insulin decreases these behaviors (Brembs et al., 2007; Yang et al., 2015; Yu et al., 2016). Accordingly, OA is released during increased physical activity, such as flight and walking, while insulin release is inhibited (Brembs et al., 2007; Suver et al., 2012; Liessem et al., 2023). Moreover, knockdown of the OAMB receptor in IPCs resulted in increased *Dilp2* expression (Luo et al., 2014; Li et al., 2016). However, our receptor expression analysis revealed that IPCs express a variety of OA receptors besides OAMB. In addition, our G-protein coupling predictions indicate that the expressed OA receptors could be excitatory and inhibitory, hence activation of OA receptors could lead to heterogenous responses in IPCs. In addition, neurons containing OA co-express other transmitters as well, in particular tyramine, Glu, GABA, and ACh (Croset et al., 2018). Therefore, activating all OANs in our experiments could lead to the release of several transmitters, which could bind to a va-

riety of receptors resulting in an overall excitatory effect. Importantly, since we activated OANs intrinsically, these co-transmitters are likely also released under natural circumstances.

In contrast, MSN and LKN activation led to an inhibition of the IPC activity in patch-clamp and calcium imaging experiments (Figure 5B). MS is known to have relaxant properties on insect muscles and leads to crop enlargement in female flies during food consumption after mating (Hadjieconomou et al., 2020). Thus, MS enables the consumption of larger meals, which is essential for mated females to account for their higher energy demands. This could be aided by the concurrent IPC inhibition we observed, since this would result in lowered insulin levels and therefore a higher feeding drive (Sudhakar et al., 2020). Interestingly, insulin-signaling also contributes to the modulation of mating in flies. Reduced insulin levels lead to a reduction of re-mating in previously mated females. Hence, the inhibitory effect of MSNs on IPCs could also act as a feedback signal to reduce premature re-mating (Wigby et al., 2011). In addition, AKH-producing cells also express receptors for MS (Braco et al., 2022). This suggests that MS could be regulating metabolic homeostasis via the modulation of insulin and AKH in the context of reproduction, where the inhibition of IPCs is one of several parallel effects mediated by MS to modulate post-mating behaviors in females.

The overall inhibitory effect of LKNs on the IPCs was more pronounced in patch-clamp recordings than in calcium imaging which is partially due to the higher sensitivity of electrophysiological recordings to membrane hyperpolarization. In calcium imaging, the IPC population activity coefficient was slightly positive, while it was strongly negative in patch-clamp recordings (Figure 5A). However, the cluster distribution shows that the inhibited IPC clusters contained the highest numbers of IPCs during LKN activation, meaning that the majority of IPCs were inhibited (Figure 5B). IPCs have also been shown to be anatomically and functionally downstream of LKNs (Zandawala et al., 2018, Yurgel et al., 2019). For example, *Lkr* knockdown specifically in IPCs impacts starvation tolerance and sleep. Specifically, a subset of LKNs increase their activity during starvation and are required for starvation-induced suppression of sleep (Yurgel et al., 2019). Insulin is also implicated in the modulation of sleep, since a loss of DILPs, especially DILP2 and DILP3, reduces sleep depth and duration (Cong et al., 2015; Brown et al., 2020). Our study supports those findings by showing that LKN activation, which would occur during starvation under normal conditions, has a strong inhibitory effect on IPCs. The resulting decreased DILP release is expected to cause a reduction of sleep, mimicking the effects of starvation mediated by LKNs.

Interestingly, with AstANs we observed different effects when comparing patch-clamp recordings with calcium imaging. In patch-clamp recordings, AstAN activation had a strong inhibitory effect on the majority of IPCs. AstA is known to inhibit feeding and promote sleep (Hentze et al., 2015; J. Chen et al., 2016; Nässel & Zandawala, 2020). Therefore, the inhibitory effect of AstAN activation on IPCs could lead to an immediate decrease in DILP release, which is then followed by a long-term reduction in IPC activity resulting from the AstA-driven cessation of food intake. However, we also recorded a fast and strong excitation in a small subset of IPCs during patch-clamp experiments. In addition, we observed a strong calcium influx in the majority of IPCs upon AstAN activation in calcium imaging experiments. Our G-protein coupling predictions can explain these heterogeneous effects, but also the differences between patch-clamp and calcium imaging. AstAR1 and AstAR2 are both predicted to couple to Gi proteins, supporting the prediction of an inhibitory effect of AstA. However, AstAR2, which is almost exclusively expressed in IPCs within the brain, is also predicted to couple to Gq subunits. Gq subunits activate cellular pathways that lead to an intracellular calcium release that subsequently causes calcium channels in the membrane to open and the influx of extracellular calcium (Dhyani et al., 2020). Therefore, the presence of AstAR2 receptors opens the possibility of a calcium increase in parallel to the overall inhibition of the IPCs (see Table S2 for more details). The heterogeneity resulting from AstAN activation in both patch-clamp and calcium imaging can be explained by heterogenous expression of receptors across individual IPCs: AstAR1 and AstAR2 are not expressed in all IPCs. It is plausible that the subset of IPCs that responded with excitation in patch-clamp recordings consists of IPCs not expressing either receptor. They could, however, receive an excitatory input via transmitters co-expressed in AstANs. Previous single cell transcriptome analyses indicated that at least some AstANs co-express ACh and glutamate (Croset et al., 2018; Nässel, 2018) and our expression analyses revealed that IPCs express receptors for these transmitters (Figure S1C). Moreover, indirect pathways from the AstANs to IPCs via interneurons could also drive excitatory responses, especially considering the long average latency of the excitatory effect (Figure 3A).

Taken together, the differences we observed for AstAN activation between patch-clamp recordings and calcium imaging emphasize the importance of utilizing parallel approaches to unravel different layers of functional effects caused by modulatory inputs to IPCs. In addition, our receptor expression analysis complements the electrophysiological data by providing valuable information about the foundation for the heterogeneous effects we observed in the functional connectivity.

IPCs form a heterogeneous population that is differentially modulated by multiple sets of neuromodulators acting in parallel

IPCs have traditionally been regarded as a homogeneous population since they appear morphologically indistinguishable and all of them express DILPs 2, 3, and 5. Recently, this dogma has been challenged by a study that found the mechanosensitive channel Piezo in only a subset of IPCs (Wang et al., 2020). We found additional proof of heterogeneity within the IPC population based on receptor expression analyses and IPC responses to MN activation. Intriguingly, cellular and functional heterogeneity also occurs in human pancreatic β-cells. This heterogeneity is assumed to be a mechanism that allows for dynamic transitions between states of high insulin production and cellular stress recovery (Gutierrez et al., 2017), which could be a general feature of insulin releasing cells.

In our study, single-nucleus transcriptomes of IPCs and anatomical receptor mapping experiments revealed that modulatory and other receptors are not uniformly expressed across the IPC population. Instead, most receptors are only expressed in subsets of IPCs. Activating MN populations while recording the IPC responses via patch-clamp revealed that the heterogeneous receptor profiles of individual IPCs have functional significance. In addition, calcium imaging experiments for selected MNs revealed that the same modulatory input led to simultaneous, heterogeneous responses across the IPC population, within the same animal. Therefore, the heterogeneity is

not based on internal state changes. The question that arises from our results is whether we investigate stochastic heterogeneity, or whether the heterogeneity is a control mechanism for insulin release. Since we demonstrated similar heterogeneous receptor expression as well as similar responses to a specific modulatory input across animals, stochastic heterogeneity, as shown in the development of photoreceptors of *Drosophila* (Anderson et al., 2017), is unlikely. For example, over 88% of IPCs expressed at least one receptor for dopamine, which matches our recordings in patch-clamp and calcium imaging closely, where the activation of DANs had an effect on 87% of IPCs. In addition, the G-protein coupling analysis accurately predicted a strong excitation of the IPC population accompanied by a weak inhibition by DA.

Since the heterogeneity occurs on the receptor level and in physiological responses, it is likely to be beneficial for the system. We hypothesize that heterogeneous activation of individual IPCs facilitates a nuanced insulin release and dynamic transitions between states of high insulin demand and recovery, perhaps comparable to the heterogeneity found in human pancreatic β-cells. A fine-tuned release from the IPCs is especially crucial when considering that insulin does not only regulate metabolic homeostasis, but also acts as a neuromodulator in the brain (Brüning et al., 2000; Root et al., 2011; Aime et al., 2012). In the olfactory systems of flies and rats, insulin reduces food searching behavior in satiated animals (Aime et al., 2012) through the inhibition of a specific subset of olfactory sensory neurons (Root et al., 2011). Therefore, insulin release needs to be adjusted to metabolic demands, and for example be reduced in foraging animals (Kim et al., 2017). We have three hypotheses for how the modulation of IPCs could alter their activity dynamics and ultimately insulin release: 1) Heterogeneous excitation and inhibition of IPCs could lead to a direct adjustment of the net output by increasing or decreasing insulin release by individual IPCs. 2) We revealed that on top of the heterogeneity, the population activity was shifted towards excitation or inhibition. Shifting a subset of IPCs into a more excited state could prime the system to enable a fast response to a secondary excitatory input (Figure 5E), for example in the context of feeding, leading to a stronger release of insulin. Receiving an additional inhibitory input in an excited state, on the other hand, would only lead to a moderate insulin release (Figure 5E). In the same fashion, shifting IPCs towards inhibition could make the system less sensitive to small changes on the input level in a generally low insulin demand state. This would enable a moderate insulin release upon arrival of a secondary excitatory input (Figure 5E). On the other hand, an additional inhibitory input would lead to a drastic shut down of IPC activity (Figure 5E) as observed during locomotion (Liessem et al., 2023). 3) The heterogeneous input could regulate the ratio of DILP2, 3, and 5 release. For example, the secretion of either DILP2 or DILP3 is selectively increased depending on the dietary conditions (Kim & Neufeld, 2015). Moreover, DILP3 expression, but not DILP2 or 5, has been tightly connected to the activity of AstANs (Hentze et al., 2015).

Generally, heterogeneity adds flexibility and stability to neuromodulatory systems. In the case of IPCs, this could allow a relatively small number of neurons to integrate a large variety of inputs to achieve flexible insulin release tailored to the current internal demands.

References

Ache, J. M., Namiki, S., Lee, A., Branson, K., & Card, G. M. (2019). State-dependent decoupling of sensory and motor circuits underlies behavioral flexibility in Drosophila. *Nat Neurosci*, *22*(7), 1132-1139. https://doi.org/10.1038/s41593-019-0413-4

Aime, P., Hegoburu, C., Jaillard, T., Degletagne, C., Garcia, S., Messaoudi, B., Thevenet, M., Lorsignol, A., Duchamp, C., Mouly, A. M., & Julliard, A. K. (2012). A physiological increase of insulin in the olfactory bulb decreases detection of a learned aversive odor and abolishes food odor-induced sniffing behavior in rats. *PLoS One*, *7*(12), e51227. https://doi.org/10.1371/journal.pone.0051227

Allen, A. M., Neville, M. C., Birtles, S., Croset, V., Treiber, C. D., Waddell, S., & Goodwin, S. F. (2020). A single-cell transcriptomic atlas of the adult Drosophila ventral nerve cord. *Elife*, *9*. https://doi.org/10.7554/eLife.54074

Anderson, C., Reiss, I., Zhou, C., Cho, A., Siddiqi, H., Mormann, B., Avelis, C. M., Deford, P., Bergland, A., Roberts, E., Taylor, J., Vasiliauskas, D., & Johnston, R. J. (2017). Natural variation in stochastic photoreceptor specification and color preference in Drosophila. *Elife*, *6*. https://doi.org/10.7554/eLife.29593

Andreatta, G., Kyriacou, C. P., Flatt, T., & Costa, R. (2018). Aminergic Signaling Controls Ovarian Dormancy in Drosophila. *Sci Rep*, *8*(1), 2030. https://doi.org/10.1038/s41598-018-20407-z

Barber, A. F., Fong, S. Y., Kolesnik, A., Fetchko, M., & Sehgal, A. (2021). Drosophila clock cells use multiple mechanisms to transmit time-of-day signals in the brain. *Proc Natl Acad Sci U S A*, *118*(10). https://doi.org/10.1073/pnas.2019826118

Bargmann, C. I., & Marder, E. (2013). From the connectome to brain function. *Nat Methods*, *10*(6), 483-490. https://doi.org/10.1038/nmeth.2451

Belgacem, Y. H., & Martin, J. R. (2006). Disruption of insulin pathways alters trehalose level and abolishes sexual dimorphism in locomotor activity in Drosophila. *J Neurobiol*, *66*(1), 19-32. https://doi.org/10.1002/neu.20193

Birse, R. T., Soderberg, J. A., Luo, J., Winther, A. M., & Nässel, D. R. (2011). Regulation of insulin-producing cells in the adult Drosophila brain via the tachykinin peptide receptor DTKR. *J Exp Biol*, *214*(Pt 24), 4201-4208. https://doi.org/10.1242/jeb.062091

Braco, J. T., Nelson, J. M., Saunders, C. J., & Johnson, E. C. (2022). Modulation of Metabolic Hormone Signaling via a Circadian Hormone and Biogenic Amine in Drosophila melanogaster. *Int J Mol Sci*, *23*(8). https://doi.org/10.3390/ijms23084266

Brembs, B., Christiansen, F., Pfluger, H. J., & Duch, C. (2007). Flight initiation and maintenance deficits in flies with genetically altered biogenic amine levels. *J Neurosci*, *27*(41), 11122-11131. https://doi.org/10.1523/JNEUROSCI.2704-07.2007

Brini, M., Cali, T., Ottolini, D., & Carafoli, E. (2014). Neuronal calcium signaling: function and dysfunction. *Cell Mol Life Sci*, *71*(15), 2787-2814. https://doi.org/10.1007/s00018-013-1550-7

Broughton, S. J., Piper, M. D. W., Ikeya, T., Bass, T. M., Jacobson, J., Driege, Y., Martinez, P., Hafen, E., Withers, D. J., Leevers, S. J., & Partridge, L. (2005). Longer lifespan, altered metabolism, and stress resistance in Drosophila from ablation of cells making insulin-like ligands. *PNAS*, *102*(8), 3105-3110.

Brown, E. B., Shah, K. D., Faville, R., Kottler, B., & Keene, A. C. (2020). Drosophila insulin-like peptide 2 mediates dietary regulation of sleep intensity. *PLoS Genet*, *16*(3), e1008270. https://doi.org/10.1371/journal.pgen.1008270

Brüning, J. C., Gautam, D., Burks, D. J., Gillette, J., Schubert, M., Orban, P. C., Klein, R., Krone, W., Müller-Wieland, D., & Kahn, C. R. (2000). Role of Brain Insulin Receptor in Control of Body Weight and Reproduction. *Science*, *289*(5487), 2122 - 2125.

Cao, C., & Brown, M. R. (2001). Localization of an insulin-like peptide in brains of two flies. *Cell Tissue Res*, *304*(2), 317-321. https://doi.org/10.1007/s004410100367

Chatterjee, N., & Perrimon, N. (2021). What fuels the fly: Energy metabolism in Drosophila and its application to the study of obesity and diabetes. *Sci Adv*, *7*(24). https://doi.org/10.1126/sciadv.abg4336

Chen, J., Reiher, W., Hermann-Luibl, C., Sellami, A., Cognigni, P., Kondo, S., Helfrich-Forster, C., Veenstra, J. A., & Wegener, C. (2016). Allatostatin A Signalling in Drosophila Regulates Feeding and Sleep and Is Modulated by PDF. *PLoS Genet*, *12*(9), e1006346. https://doi.org/10.1371/journal.pgen.1006346

Chen, T. W., Wardill, T. J., Sun, Y., Pulver, S. R., Renninger, S. L., Baohan, A., Schreiter, E. R., Kerr, R. A., Orger, M. B., Jayaraman, V., Looger, L. L., Svoboda, K., & Kim, D. S. (2013). Ultrasensitive fluorescent proteins for imaging neuronal activity. *Nature*, *499*(7458), 295-300. https://doi.org/10.1038/nature12354

Chen, X., Rahman, R., Guo, F., & Rosbash, M. (2016). Genome-wide identification of neuronal activity-regulated genes in Drosophila. *Elife*, *5*. https://doi.org/10.7554/eLife.19942

Cong, X., Wang, H., Liu, Z., He, C., An, C., & Zhao, Z. (2015). Regulation of Sleep by Insulin-like Peptide System in Drosophila melanogaster. *Sleep*, *38*(7), 1075-1083. https://doi.org/10.5665/sleep.4816

Croset, V., Treiber, C. D., & Waddell, S. (2018). Cellular diversity in the Drosophila midbrain revealed by single-cell transcriptomics. *Elife*, *7*. https://doi.org/10.7554/eLife.34550

Daur, N., Nadim, F., & Bucher, D. (2016). The complexity of small circuits: the stomatogastric nervous system. *Curr Opin Neurobiol*, *41*, 1-7. https://doi.org/10.1016/j.conb.2016.07.005

Deng, B., Li, Q., Liu, X., Cao, Y., Li, B., Qian, Y., Xu, R., Mao, R., Zhou, E., Zhang, W., Huang, J., & Rao, Y. (2019). Chemoconnectomics: Mapping Chemical Transmission in Drosophila. *Neuron*, *101*(5), 876-893 e874. https://doi.org/10.1016/j.neuron.2019.01.045

Dhyani, V., Gare, S., Gupta, R. K., Swain, S., Venkatesh, K. V., & Giri, L. (2020). GPCR mediated control of calcium dynamics: A systems perspective. *Cell Signal*, *74*, 109717. https://doi.org/10.1016/j.cellsig.2020.109717

Dorkenwald, S., Matsliah, A., Sterling, A. R., Schlegel, P., Yu, S. C., McKellar, C. E., Lin, A., Costa, M., Eichler, K., Yin, Y., Silversmith, W., Schneider-Mizell, C., Jordan, C. S., Brittain, D., Halageri, A., Kuehner, K., Ogedengbe, O., Morey, R., Gager, J., Kruk, K., Perlman, E., Yang, R., Deutsch, D., Bland, D., Sorek, M., Lu, R., Macrina, T., Lee, K., Bae, J. A., Mu, S., Nehoran, B., Mitchell, E., Popovych, S., Wu, J., Jia, Z., Castro, M., Kemnitz, N., Ih, D., Bates, A. S., Eckstein, N., Funke, J., Collman, F., Bock, D. D., Jefferis, G., Seung, H. S., Murthy, M., & FlyWire, C. (2023). Neuronal wiring diagram of an adult brain. *bioRxiv*. https://doi.org/10.1101/2023.06.27.546656

Edelstein, A. D., Tsuchida, M. A., Amodaj, N., Pinkard, H., Vale, R. D., & Stuurman, N. (2014). Advanced methods of microscope control using muManager software. *J Biol Methods*, *1*(2), e10. https://doi.org/10.14440/jbm.2014.36

Evans, P. D., & Maqueira, B. (2005). Insect octopamine receptors: a new classification scheme based on studies of cloned Drosophila G-protein coupled receptors. *Invert Neurosci*, *5*(3-4), 111-118. https://doi.org/10.1007/s10158-005-0001-z

Fernandez, A. M., & Torres-Aleman, I. (2012). The many faces of insulin-like peptide signalling in the brain. *Nat Rev Neurosci*, *13*(4), 225-239. https://doi.org/10.1038/nrn3209

Friggi-Grelin, F., Coulom, H., Meller, M., Gomez, D., Hirsh, J., & Birman, S. (2003). Targeted gene expression in Drosophila dopaminergic cells using regulatory sequences from tyrosine hydroxylase. *J Neurobiol*, *54*(4), 618-627. https://doi.org/10.1002/neu.10185

Garofalo, R. S. (2002). Genetic analysis of insulin signaling in Drosophila. *Trends in Endocrinology & Metabolism*, *13*(4), 156 - 162.

Gough, C. S., Fairlamb, G. M., Bell, P., Nachman, R. J., Audsley, N., & Isaac, R. E. (2017). Peptidergic control in a fruit crop pest: The spotted-wing drosophila, Drosophila suzukii. *PLoS One*, *12*(11), e0188021. https://doi.org/10.1371/journal.pone.0188021

Gouwens, N. W., & Wilson, R. I. (2009). Signal Propagation in Drosophila Central Neurons. *The Journal of Neuroscience*, *29*(19), 6239. https://doi.org/10.1523/JNEUROSCI.0764-09.2009

Griffith, L. C. (2012). Identifying behavioral circuits in Drosophila melanogaster: moving targets in a flying insect. *Curr Opin Neurobiol*, *22*(4), 609-614. https://doi.org/10.1016/j.conb.2012.01.002

Gutierrez, G. D., Gromada, J., & Sussel, L. (2017). Heterogeneity of the Pancreatic Beta Cell. *Front Genet*, *8*, 22. https://doi.org/10.3389/fgene.2017.00022

Hadjieconomou, D., King, G., Gaspar, P., Mineo, A., Blackie, L., Ameku, T., Studd, C., de Mendoza, A., Diao, F., White, B. H., Brown, A. E. X., Placais, P. Y., Preat, T., & Miguel-Aliaga, I. (2020). Enteric neurons increase maternal food intake during reproduction. *Nature*, *587*(7834), 455-459. https://doi.org/10.1038/s41586-020-2866-8

Hallier, B., Schiemann, R., Cordes, E., Vitos-Faleato, J., Walter, S., Heinisch, J. J., Malmendal, A., Paululat, A., & Meyer, H. (2016). Drosophila neprilysins control insulin signaling and food intake via cleavage of regulatory peptides. *Elife*, *5*. https://doi.org/10.7554/eLife.19430

Hao, Y., Hao, S., Andersen-Nissen, E., Mauck, W. M., 3rd, Zheng, S., Butler, A., Lee, M. J., Wilk, A. J., Darby, C., Zager, M., Hoffman, P., Stoeckius, M., Papalexi, E., Mimitou, E. P., Jain, J., Srivastava, A., Stuart, T., Fleming, L. M., Yeung, B., Rogers, A. J., McElrath, J. M., Blish, C. A., Gottardo, R., Smibert, P., & Satija, R. (2021). Integrated analysis of multimodal single-cell data. *Cell*, *184*(13), 3573-3587 e3529. https://doi.org/10.1016/j.cell.2021.04.048

Hector, C. E., Bretz, C. A., Zhao, Y., & Johnson, E. C. (2009). Functional differences between two CRF-related diuretic hormone receptors in Drosophila. *J Exp Biol*, *212*(19), 3142-3147. https://doi.org/10.1242/jeb.033175

Hentze, J. L., Carlsson, M. A., Kondo, S., Nässel, D. R., & Rewitz, K. F. (2015). The Neuropeptide Allatostatin A Regulates Metabolism and Feeding Decisions in Drosophila. *Sci Rep*, *5*, 11680. https://doi.org/10.1038/srep11680

Kapan, N., Lushchak, O. V., Luo, J., & Nässel, D. R. (2012). Identified peptidergic neurons in the Drosophila brain regulate insulin-producing cells, stress responses and metabolism by coexpressed short neuropeptide F and corazonin. *Cell Mol Life Sci*, *69*(23), 4051-4066. https://doi.org/10.1007/s00018-012-1097-z

Kim, J., & Neufeld, T. P. (2015). Dietary sugar promotes systemic TOR activation in Drosophila through AKH-dependent selective secretion of Dilp3. *Nat Commun*, *6*, 6846. https://doi.org/10.1038/ncomms7846

Kim, S. M., Su, C. Y., & Wang, J. W. (2017). Neuromodulation of Innate Behaviors in Drosophila. *Annu Rev Neurosci*, *40*, 327-348. https://doi.org/10.1146/annurev-neuro-072116-031558

Kondo, S., Takahashi, T., Yamagata, N., Imanishi, Y., Katow, H., Hiramatsu, S., Lynn, K., Abe, A., Kumaraswamy, A., & Tanimoto, H. (2020). Neurochemical Organization of the Drosophila Brain Visualized by Endogenously Tagged Neurotransmitter Receptors. *Cell Rep*, *30*(1), 284-297 e285. https://doi.org/10.1016/j.celrep.2019.12.018

Larsen, M. J., Burton, K. J., Zantello, M. R., Smith, V. G., Lowery, D. L., & Kubiak, T. M. (2001). Type A allatostatins from Drosophila melanogaster and Diplotera puncata activate two Drosophila allatostatin receptors, DAR-1 and DAR-2, expressed in CHO cells. *Biochem Biophys Res Commun*, *286*(5), 895-901. https://doi.org/10.1006/bbrc.2001.5476

Li, H., Janssens, J., De Waegeneer, M., Kolluru, S. S., Davie, K., Gardeux, V., Saelens, W., David, F. P. A., Brbic, M., Spanier, K., Leskovec, J., McLaughlin, C. N., Xie, Q., Jones, R. C., Brueckner, K., Shim, J., Tattikota, S. G., Schnorrer, F., Rust, K., Nystul, T. G., Carvalho-Santos, Z., Ribeiro, C., Pal, S., Mahadevaraju, S., Przytycka, T. M., Allen, A. M., Goodwin, S. F., Berry, C. W., Fuller, M. T., White-Cooper, H., Matunis, E. L., DiNardo, S., Galenza, A., O'Brien, L. E., Dow, J. A. T., sign, F. C. A. C. s., Jasper, H., Oliver, B., Perrimon, N., Deplancke, B., Quake, S. R., Luo, L., Aerts, S., Agarwal, D., Ahmed-Braimah, Y., Arbeitman, M., Ariss, M. M., Augsburger, J., Ayush, K., Baker, C. C., Banisch, T., Birker, K., Bodmer, R., Bolival, B., Brantley, S. E., Brill, J. A., Brown, N. C., Buehner, N. A., Cai, X. T., Cardoso-Figueiredo, R., Casares, F., Chang, A., Clandinin, T. R., Crasta, S., Desplan, C., Detweiler, A. M., Dhakan, D. B., Dona, E., Engert, S., Floc'hlay, S., George, N., Gonzalez-Segarra, A. J., Groves, A. K., Gumbin, S., Guo, Y., Harris, D. E., Heifetz, Y., Holtz, S. L., Horns, F., Hudry, B., Hung, R. J., Jan, Y. N., Jaszczak, J. S., Jefferis, G., Karkanias, J., Karr, T. L., Katheder, N. S., Kezos, J., Kim, A. A., Kim, S. K., Kockel, L., Konstantinides, N., Kornberg, T. B., Krause, H. M., Labott, A. T., Laturney, M., Lehmann, R., Leinwand, S., Li, J., Li, J. S. S., Li, K., Li, K., Li, L., Li, T., Litovchenko, M., Liu, H. H., Liu, Y., Lu, T. C., Manning, J., Mase, A., Matera-Vatnick, M., Matias, N. R., McDonough-Goldstein, C. E., McGeever, A., McLachlan, A. D., Moreno-Roman, P., Neff, N., Neville, M., Ngo, S., Nielsen, T., O'Brien, C. E., Osumi-Sutherland, D., Ozel, M. N., Papatheodorou, I., Petkovic, M., Pilgrim, C., Pisco, A. O., Reisenman, C., Sanders, E. N., Dos Santos, G., Scott, K., Sherlekar, A., Shiu, P., Sims, D., Sit, R. V., Slaidina, M., Smith, H. E., Sterne, G., Su, Y. H., Sutton, D., Tamayo, M., Tan, M., Tastekin, I., Treiber, C., Vacek, D., Vogler, G., Waddell, S., Wang, W., Wilson, R. I., Wolfner, M. F., Wong, Y. E., Xie, A., Xu, J., Yamamoto, S., Yan, J., Yao, Z., Yoda, K., Zhu, R., & Zinzen, R. P. (2022). Fly Cell Atlas: A single-nucleus transcriptomic atlas of the adult fruit fly. *Science*, *375*(6584), eabk2432. https://doi.org/10.1126/science.abk2432

Li, Q., & Gong, Z. (2015). Cold-sensing regulates Drosophila growth through insulin-producing cells. *Nat Commun*, *6*, 10083. https://doi.org/10.1038/ncomms10083

Li, Y., Hoffmann, J., Li, Y., Stephano, F., Bruchhaus, I., Fink, C., & Roeder, T. (2016). Octopamine controls starvation resistance, life span and metabolic traits in Drosophila. *Sci Rep*, *6*, 35359. https://doi.org/10.1038/srep35359

Liessem, S., Held, M., Bisen, R. S., Haberkern, H., Lacin, H., Bockemühl, T., & Ache, J. M. (2023). Behavioral state-dependent modulation of insulin-producing cells in Drosophila. *Curr Biol*. https://doi.org/10.1016/j.cub.2022.12.005

Lin, H. H., Kuang, M. C., Hossain, I., Xuan, Y., Beebe, L., Shepherd, A. K., Rolandi, M., & Wang, J. W. (2022). A nutrient-specific gut hormone arbitrates between courtship and feeding. *Nature*, *602*(7898), 632-638. https://doi.org/10.1038/s41586-022-04408-7

Luo, J., Becnel, J., Nichols, C. D., & Nässel, D. R. (2012). Insulin-producing cells in the brain of adult Drosophila are regulated by the serotonin 5-

HT1A receptor. *Cell Mol Life Sci*, *69*(3), 471-484. https://doi.org/10.1007/s00018-011-0789-0

Luo, J., Lushchak, O. V., Goergen, P., Williams, M. J., & Nässel, D. R. (2014). Drosophila insulin-producing cells are differentially modulated by serotonin and octopamine receptors and affect social behavior. *PLoS One*, *9*(6), e99732. https://doi.org/10.1371/journal.pone.0099732

Marder, E. (2012). Neuromodulation of neuronal circuits: back to the future. *Neuron*, *76*(1), 1-11. https://doi.org/10.1016/j.neuron.2012.09.010

Musselman, L. P., Fink, J. L., Narzinski, K., Ramachandran, P. V., Hathiramani, S. S., Cagan, R. L., & Baranski, T. J. (2011). A high-sugar diet produces obesity and insulin resistance in wild-type Drosophila. *Dis Model Mech*, *4*(6), 842-849. https://doi.org/10.1242/dmm.007948

Nässel, D. R. (2012). Insulin-producing cells and their regulation in physiology and behavior of Drosophila. *Canadian Journal of Zoology*, *90*(4), 476-488. https://doi.org/10.1139/z2012-009

Nässel, D. R. (2018). Substrates for Neuronal Cotransmission With Neuropeptides and Small Molecule Neurotransmitters in Drosophila. *Front Cell Neurosci*, *12*, 83. https://doi.org/10.3389/fncel.2018.00083

Nässel, D. R., Kubrak, O. I., Liu, Y., Luo, J., & Lushchak, O. V. (2013). Factors that regulate insulin producing cells and their output in Drosophila. *Front Physiol*, *4*, 252. https://doi.org/10.3389/fphys.2013.00252

Nässel, D. R., & Vanden Broeck, J. (2016). Insulin/IGF signaling in Drosophila and other insects: factors that regulate production, release and post-release action of the insulin-like peptides. *Cell Mol Life Sci*, *73*(2), 271-290. https://doi.org/10.1007/s00018-015-2063-3

Nässel, D. R., & Zandawala, M. (2019). Recent advances in neuropeptide signaling in Drosophila, from genes to physiology and behavior. *Prog Neurobiol*, *179*, 101607. https://doi.org/10.1016/j.pneurobio.2019.02.003

Nässel, D. R., & Zandawala, M. (2020). Hormonal axes in Drosophila: regulation of hormone release and multiplicity of actions. *Cell Tissue Res*, *382*(2), 233-266. https://doi.org/10.1007/s00441-020-03264-z

Nässel, D. R., & Zandawala, M. (2022). Endocrine cybernetics: neuropeptides as molecular switches in behavioural decisions. *Open Biol*, *12*(7), 220174. https://doi.org/10.1098/rsob.220174

Oh, Y., Lai, J. S., Mills, H. J., Erdjument-Bromage, H., Giammarinaro, B., Saadipour, K., Wang, J. G., Abu, F., Neubert, T. A., & Suh, G. S. B. (2019). A glucose-sensing neuron pair regulates insulin and glucagon in Drosophila. *Nature*, *574*(7779), 559-564. https://doi.org/10.1038/s41586-019-1675-4

Ormazabal, V., Nair, S., Elfeky, O., Aguayo, C., Salomon, C., & Zuniga, F. A. (2018). Association between insulin resistance and the development of cardiovascular disease. *Cardiovasc Diabetol*, *17*(1), 122. https://doi.org/10.1186/s12933-018-0762-4

Partridge, L., Alic, N., Bjedov, I., & Piper, M. D. (2011). Ageing in Drosophila: the role of the insulin/Igf and TOR signalling network. *Exp Gerontol*, *46*(5), 376-381. https://doi.org/10.1016/j.exger.2010.09.003

Prentki, M., Matschinsky, F. M., & Madiraju, S. R. (2013). Metabolic signaling in fuel-induced insulin secretion. *Cell Metab*, *18*(2), 162-185. https://doi.org/10.1016/j.cmet.2013.05.018

Reinhard, N., Fukuda, A., Manoli, G., Derksen, E., Saito, A., Möller, G., Sekiguchi, M., Rieger, D., Helfrich-Förster, C., Yoshii, T., & Zandawala, M. (2023). Synaptic and peptidergic connectomes of the Drosophila circadian clock. *bioRxiv*, *2023.09.11.557222*. https://doi.org/10.1101/2023.09.11.557222

Root, C. M., Ko, K. I., Jafari, A., & Wang, J. W. (2011). Presynaptic facilitation by neuropeptide signaling mediates odor-driven food search. *Cell*, *145*(1), 133-144. https://doi.org/10.1016/j.cell.2011.02.008

Rosikon, K. D., Bone, M. C., & Lawal, H. O. (2023). Regulation and modulation of biogenic amine neurotransmission in Drosophila and Caenorhabditis elegans. *Front Physiol*, *14*, 970405. https://doi.org/10.3389/fphys.2023.970405

Scheffer, L. K., Xu, C. S., Januszewski, M., Lu, Z., Takemura, S. Y., Hayworth, K. J., Huang, G. B., Shinomiya, K., Maitlin-Shepard, J., Berg, S., Clements, J., Hubbard, P. M., Katz, W. T., Umayam, L., Zhao, T., Ackerman, D., Blakely, T., Bogovic, J., Dolafi, T., Kainmueller, D., Kawase, T., Khairy, K. A., Leavitt, L., Li, P. H., Lindsey, L., Neubarth, N., Olbris, D. J., Otsuna, H., Trautman, E. T., Ito, M., Bates, A. S., Goldammer, J., Wolff, T., Svirskas, R., Schlegel, P., Neace, E., Knecht, C. J., Alvarado, C. X., Bailey, D. A., Ballinger, S., Borycz, J. A., Canino, B. S., Cheatham, N., Cook, M., Dreher, M., Duclos, O., Eubanks, B., Fairbanks, K., Finley, S., Forknall, N., Francis, A., Hopkins, G. P., Joyce, E. M., Kim, S., Kirk, N. A., Kovalyak, J., Lauchie, S. A., Lohff, A., Maldonado, C., Manley, E. A., McLin, S., Mooney, C., Ndama, M., Ogundeyi, O., Okeoma, N., Ordish, C., Padilla, N., Patrick, C. M., Paterson, T., Phillips, E. E., Phillips, E. M., Rampally, N., Ribeiro, C., Robertson, M. K., Rymer, J. T., Ryan, S. M., Sammons, M., Scott, A. K., Scott, A. L., Shinomiya, A., Smith, C., Smith, K., Smith, N. L., Sobeski, M. A., Suleiman, A., Swift, J., Takemura, S., Talebi, I., Tarnogorska, D., Tenshaw, E., Tokhi, T., Walsh, J. J., Yang, T., Horne, J. A., Li, F., Parekh, R., Rivlin, P. K., Jayaraman, V., Costa, M., Jefferis, G. S., Ito, K., Saalfeld, S., George, R., Meinertzhagen, I. A., Rubin, G. M., Hess, H. F., Jain, V., & Plaza, S. M. (2020). A connectome and analysis of the adult Drosophila central brain. *Elife*, *9*. https://doi.org/10.7554/eLife.57443

Schlegel, P., Yin, Y., Bates, A. S., Dorkenwald, S., Eichler, K., Brooks, P., Han, D. S., Gkantia, M., Dos Santos, M., Munnelly, E. J., Badalamente, G., Capdevila, L. S., Sane, V. A., Pleijzier, M. W., Tamimi, I. F. M., Dunne, C. R., Salgarella, I., Javier, A., Fang, S., Perlman, E., Kazimiers, T., Jagannathan, S. R., Matsliah, A., Sterling, A. R., Yu, S. C., McKellar, C. E., FlyWire, C., Costa, M., Seung, H. S., Murthy, M., Hartenstein, V., Bock, D. D., & Jefferis, G. (2023). Whole-brain annotation and multi-connectome cell typing quantifies circuit stereotypy in Drosophila. *bioRxiv*. https://doi.org/10.1101/2023.06.27.546055

Seelig, J. D., & Jayaraman, V. (2015). Neural dynamics for landmark orientation and angular path integration. *Nature*, *521*(7551), 186-191. https://doi.org/10.1038/nature14446

Siju, K. P., De Backer, J. F., & Grunwald Kadow, I. C. (2021). Dopamine modulation of sensory processing and adaptive behavior in flies. *Cell Tissue Res*, *383*(1), 207-225. https://doi.org/10.1007/s00441-020-03371-x

Söderberg, J. A., Carlsson, M. A., & Nässel, D. R. (2012). Insulin-Producing Cells in the Drosophila Brain also Express Satiety-Inducing Cholecystokinin-Like Peptide, Drosulfakinin. *Front Endocrinol (Lausanne)*, *3*, 109. https://doi.org/10.3389/fendo.2012.00109

Sriram, K., Wiley, S. Z., Moyung, K., Gorr, M. W., Salmeron, C., Marucut, J., French, R. P., Lowy, A. M., & Insel, P. A. (2019). Detection and Quantification of GPCR mRNA: An Assessment and Implications of Data from High-Content Methods. *ACS Omega*, *4*(16), 17048-17059. https://doi.org/10.1021/acsomega.9b02811

Sudhakar, S. R., Pathak, H., Rehman, N., Fernandes, J., Vishnu, S., & Varghese, J. (2020). Insulin signalling elicits hunger-induced feeding in Drosophila. *Dev Biol*, *459*(2), 87-99. https://doi.org/10.1016/j.ydbio.2019.11.013

Suver, M. P., Mamiya, A., & Dickinson, M. H. (2012). Octopamine neurons mediate flight-induced modulation of visual processing in Drosophila. *Curr Biol*, *22*(24), 2294-2302. https://doi.org/10.1016/j.cub.2012.10.034

Taghert, P. H., & Nitabach, M. N. (2012). Peptide neuromodulation in invertebrate model systems. *Neuron*, *76*(1), 82-97. https://doi.org/10.1016/j.neuron.2012.08.035

Takeda, K., Okumura, T., Terahata, M., Yamaguchi, M., Taniguchi, K., & Adachi-Yamada, T. (2018). Drosophila Peptide Hormones Allatostatin A and Diuretic Hormone 31 Exhibiting Complementary Gradient Distribution in Posterior Midgut Antagonistically Regulate Midgut Senescence and Adult Lifespan. *Zoolog Sci*, *35*(1), 75-85. https://doi.org/10.2108/zs160210

Tatar, M., Bartke, A., & Antebi, A. (2003). The Endocrine Regulation of Aging by Insulin-like Signals. *Science*, *299*(5611), 1346-1351.

Veenstra, J. A., Agricola, H. J., & Sellami, A. (2008). Regulatory peptides in fruit fly midgut. *Cell Tissue Res*, *334*(3), 499-516. https://doi.org/10.1007/s00441-008-0708-3

Venkiteswaran, G., & Hasan, G. (2009). Intracellular Ca2+ signaling and store-operated Ca2+ entry are required in Drosophila neurons for flight. *PNAS*, *106*(25). https://doi.org/10.1073/pnas.0902982106

Wang, P., Jia, Y., Liu, T., Jan, Y. N., & Zhang, W. (2020). Visceral Mechano-sensing Neurons Control Drosophila Feeding by Using Piezo as a Sensor. *Neuron*, *108*(4), 640-650 e644. https://doi.org/10.1016/j.neuron.2020.08.017

Wigby, S., Slack, C., Grönke, S., Martinez, P., Calboli, F. C., Chapman, T., & Partridge, L. (2011). Insulin signalling regulates remating in female Drosophila. *Proc Biol Sci*, *278*(1704), 424-431. https://doi.org/10.1098/rspb.2010.1390

Wu, S., Guo, C., Zhao, H., Sun, M., Chen, J., Han, C., Peng, Q., Qiao, H., Peng, P., Liu, Y., Luo, S. D., & Pan, Y. (2019). Drosulfakinin signaling in fruitless circuitry antagonizes P1 neurons to regulate sexual arousal in Drosophila. *Nat Commun*, *10*(1), 4770. https://doi.org/10.1038/s41467-019-12758-6

Yamamoto, S., & Seto, E. S. (2014). Dopamine Dynamics and Signaling in Drosophila: An Overview of Genes, Drugs and Behavioral Paradigms. *Exp Anim*, *63*(2), 107-119.

Yang, Z., Yu, Y., Zhang, V., Tian, Y., Qi, W., & Wang, L. (2015). Octopamine mediates starvation-induced hyperactivity in adult Drosophila. *Proc Natl Acad Sci U S A*, *112*(16), 5219-5224. https://doi.org/10.1073/pnas.1417838112

Yu, Y., Huang, R., Ye, J., Zhang, V., Wu, C., Cheng, G., Jia, J., & Wang, L. (2016). Regulation of starvation-induced hyperactivity by insulin and glucagon signaling in adult Drosophila. *Elife*, *5*. https://doi.org/10.7554/eLife.15693

Yurgel, M. E., Kakad, P., Zandawala, M., Nässel, D. R., Godenschwege, T. A., & Keene, A. C. (2019). A single pair of leucokinin neurons are modulated by feeding state and regulate sleep-metabolism interactions. *PLoS Biol*, *17*(2), e2006409. https://doi.org/10.1371/journal.pbio.2006409

Zandawala, M., Nguyen, T., Balanya Segura, M., Johard, H. A. D., Amcoff, M., Wegener, C., Paluzzi, J. P., & Nässel, D. R. (2021). A neuroendocrine pathway modulating osmotic stress in Drosophila. *PLoS Genet*, *17*(3), e1009425. https://doi.org/10.1371/journal.pgen.1009425

Zandawala, M., Yurgel, M. E., Texada, M. J., Liao, S., Rewitz, K. F., Keene, A. C., & Nässel, D. R. (2018). Modulation of Drosophila post-feeding physiology and behavior by the neuropeptide leucokinin. *PLoS Genet*, *14*(11), e1007767. https://doi.org/10.1371/journal.pgen.1007767

Zheng, Z., Lauritzen, J. S., Perlman, E., Robinson, C. G., Nichols, M., Milkie, D., Torrens, O., Price, J., Fisher, C. B., Sharifi, N., Calle-Schuler, S. A., Kmecova, L., Ali, I. J., Karsh, B., Trautman, E. T., Bogovic, J. A., Hanslovsky, P., Jefferis, G., Kazhdan, M., Khairy, K., Saalfeld, S., Fetter, R. D., & Bock, D. D. (2018). A Complete Electron Microscopy Volume of the Brain of Adult Drosophila melanogaster. *Cell*, *174*(3), 730-743 e722. https://doi.org/10.1016/j.cell.2018.06.019

Author contributions

Writing – original draft, M.H., M.Z., and J.M.A.; writing – review & editing, M.H., R.S.B., M.Z., A.S.C., I.S.B., S.H., S.L., F.C.-M., and J.M.A.; patch-clamp recordings, R.S.B., A.S.C., S.L., F.C.-M.; calcium imaging, M.H. and I.S.B.; receptor expression, M.Z. and S.H.; anatomy, M.H., R.S.B., and S.H.; software, M.H., M.Z., F.C.-M., and J.M.A.; formal analysis, M.H., R.S.B., M.Z., I.S.B., F.C.-M. and J.M.A; supervision, M.Z. and J.M.A.; project conceptualization, M.H., M.Z., and J.M.A; project administration, J.M.A; funding acquisition, M.Z. and J.M.A.

Acknowledgements

We thank Haluk Lacin (University of Missouri-Kansas City) for providing fly-lines for activation experiments, Jan A. Veenstra (University of Bordeaux) for providing the DILP-2 antibody, and Susan Morton for providing the RFP antibody. We are grateful to Konrad Öchsner for technical assistance and to Charlotte Helfrich-Förster and Wolfgang Rössler (all Julius-Maximilians-Universität of Würzburg) for sharing resources; We also thank Nicole Enslinger for preliminary calcium imaging experiments and Emilia Derksen (both JMU) for technical support. We are grateful to Dick R. Nässel (Stockholm University), Tanja A. Godenschwege (Florida Atlantic University), Mattias Alenius (Umeå University), and Chris J. Dallmann (JMU) for valuable feedback on the manuscript. This work was supported by a grant from the Deutsche Forschungsgemeinschaft (DFG) to J.M.A. via the Emmy Noether program (DFG AC 371/1-1), by a grant from the DFG to J.M.A. as part of the NSF/CIHR/DFG/FRQ/UKRI-MRC Next Generation Networks for Neuroscience (Neuronex) Program (DFG AC 371/2-1), by a grant to J.M.A. from the Bavaria California Technology Center (BaCaTec), and by a grant from the DFG to M.Z. (DFG; ZA1296/1-1).

Competing interest statement

The authors declare no competing interests, financial or otherwise.

Materials and Methods

Fly husbandry

All flies were reared on standard fly food (cornmeal-agar-molasses medium) and kept in a climate chamber at 60% relative humidity, 25°C, and a 12h:12h light/dark cycle. Experiments were performed on mated females 3 – 6 days after eclosion. For experiments with optogenetic activation of CsChrimson, 300 µM all-trans-retinal (R2500, Sigma-Aldrich, Steinheim, Germany) was added to standard fly food and experimental flies were kept on that food after eclosion in darkness until usage.

Fly genotypes

Table 1 shows all genotypes used for anatomical receptor mapping and Table 2 shows the genotypes used for activation experiments as well as brain and VNC anatomical labeling.

Table 1: Fly genotypes for anatomical mapping

Line trivial name	Genotype	Source
UAS-NLS-mCherry	w[*]; P{w[+mC]=UAS-mCherry.NLS}2; MKRS/TM6B, Tb[1]	BDSC #38425
Oct-TyrR-T2A-GAL4	TI{RFP[3xP3.cUa]=2A-GAL4}Oct-TyrR[2A-GAL4.KI]	BDSC #86138
5HT7-T2A-GAL4	TI{2A-GAL4}5-HT7[2A-GAL4]	BDSC #84592
Oct-alpha2R-T2A-GAL4	w[*]; TI{2A-GAL4}Octalpha2R[2A-GAL4]	BDSC #84610
AstAR1-T2A-GAL4		(Deng et al., 2019)
MsR1-(B)-T2A-GAL4	w[*]; TI{2A-GAL4}MsR1[2A-B.GAL4]/TM3, Sb[1]	BDSC #84653
MsR2-(C)-T2A-GAL4	w[*];TI{RFP[3xP3.cUa]=TI}MsR2[attP]	BDSC #84525 (Deng et al., 2019)
AstAR2-(A/C)-T2A-GAL4	w[*]; TI{2A-GAL4}AstA-R2[2A-AC.GAL4]/TM3, Sb[1]	BDSC #84594
sNPFR-T2A-GAL4	w[*]; TI{2A-GAL4}sNPF-R[2A-GAL4]/TM6B, Tb[1]	BDSC #84691
CCKLR17D1-T2A-GAL4	w[*] TI{2A-GAL4}CCKLR-17D1[2A-GAL4]	BDSC #84605
CrzR-T2A-GAL4	yw;;CrzR-T2A-GAL4	(Kondo et al., 2020)
Dh31R-(A/B/C)-T2A-GAL4	TI{2A-GAL4}Dh31-R[2A-ABC.GAL4]	BDSC #84625
Dop2R-T2A-GAL4	w[*] TI{2A-GAL4}Dop2R[2A-GAL4]	BDSC #84628
LkR-GAL4 Knock-in mutant	w1118; Lkr-GAL4 ^{CC9} (mutant)	(Zandawala et al., 2018)
Oct-alpha2R-Trojan-GAL4	y[1] w[*]; Mi{Trojan-GAL4.0}Octalpha2R[MI10227-TG4.0]/TM3, Sb[1] Ser[1]	BDSC #67636
5-HT1A-T2A-GAL4	TI{2A-GAL4}5-HT1A[2A-GAL4]	BDSC #84588

Table 2: Fly genotypes for activation experiments and expression analysis

Line trivial name	Genotype	Source
DILP2::GFP; UAS-CsChrimson (HL2)	+/+: R96A08-LexA-p65-vk37::LexOp-DILP2::GFP; 20x-UAS-CsChrimson-attp2/TM6b, Tb	Dr. Haluk Lacin
DILP2-GCaMP6m::UAS CsChrimson (HL7)	+/+; R96A08-LexA-p65-vk37/CyO; LexOp-GCaMP6m-vk5, 20X-UAS-CsChrimson.mVenus-su(Hw) attp1/TM6	Dr. Haluk Lacin
TH-GAL4	w[*]; P{w[+mC]=ple-GAL4.F}3	(Friggi-Grelin et al., 2003)
AstA-GAL4	+/+; +/+; DKI0090 T{2A-GAL4}AstA[2A-GAL4]	BDSC #84593
Tdc2-GAL4	+/+; P{Tdc2-GAL4.C}2; +/+	BDSC #9313
LK-GAL4	w[1118]; P{w[+mC]=Lk-GAL4.TH}2M; +/+	BDSC # 51993
MS-GAL4	w[1118]; P{w[+mC]=Ms-GAL4.TH}6Ma; +/+	BDSC #51986
AKH-GAL4	y[1]w[*]; +/+; P{w[+mC]=Akh-gal4.L}3	BDSC #25684
TK-GAL4	w[1118]; P{w[+mC]=TK-GAL4.TH}2Ma; +/+	BDSC #51973
sNPF-GAL4	P{w[+mC]=sNPF-GAL4.TH}2; +/+; +/+	BDSC #51991
DH31-GAL4	+/+; +/+; P{w[+mC]=DH31-GAL4.TH}2M	BDSC #51988
TrH-GAL4	+/+; +/+; DkI0247 TrH-GAL4	CG9122, Prof. Dr. Yi Rao
GFP-p10	w[*]; P{10XUAS-IVS-GFP}attP2	BDSC #32201

BDSC = Bloomington *Drosophila* Stock Center

Immunohistochemistry

Anatomical receptor mapping

Flies of the F1 generation from crosses with GAL4 lines from Table 1 and UAS-NLS-mCherry were used for anatomical receptor mapping. We primarily used the recently generated receptor-T2A-GAL4 knock-in lines (Deng et al., 2019; Kondo et al., 2020) to drive expression of nuclear mCherry. Since the T2A-GAL4 knock-in lines were generated by inserting the T2A-GAL4 coding sequence right before the stop codon for the gene, an accurate expression can be assumed since the GAL4 is expressed in the same temporal and spatial patterns, and at similar levels, as the native receptor. Flies were prefixed at room temperature for 2.5 hours in a 2 mL tube with 1.5 mL 4% paraformaldehyde and 20 µL 0.5% PBT (phosphate-buffered saline with 0.5% TritonX-100; Sigma-Aldrich, Steinheim, Germany). The fixed flies were washed 4 × 15 minutes each with 0.5% PBT. Brains were dissected afterwards and collected directly in 400 µL blocking solution (5% NGS in PBT) and incubated for 1.5 hours to block non-specific binding sites. Next, samples were incubated in primary antibodies (Table 3) diluted in blocking solution for 48 hours at 4°C. Afterwards, the brains were washed 4 × 15 minutes each in PBST at room temperature before they were incubated in the secondary antibodies (Table 3) for 48 hours at 4°C. Next, the samples were washed for 4 × 15 minutes in PBT, followed by two final washing steps in PBS for 15 minutes each before they were mounted in Fluoro mount-G (Invitrogen, Waltham, MA, USA). Z-stacks were acquired using a Leica TCS SPE confocal microscope (Leica Microsystems, Wetzlar, Germany) equipped with Leica Microsystems LAS AF software, a photo-multiplier tube, and 488, 532, and 635 nm solid-state lasers for excitation. We used a 20× glycerol immersion objective for whole-mount scans and 40× oil immersion objective for detailed images. All images were captured at a resolution of 1024×1024 pixels. To reduce background noise, all frames were captured two to three times and then averaged. Images were analyzed with ImageJ.

Expression analysis of driver lines used for activation experiments

To extract the brain and VNC from flies of the driver lines we used in the optogenetic activation experiments, flies were anesthetized on ice and then fixed in 4% PFA in 0.1 M PBS for 3 hours followed by three subsequent washes in 0.1 M PBS. They were then dissected in 0.1 M PBS at room temperature. Prior to dissection, each fly was shortly submerged in 70% ethanol for ~30s. The dissected brains were then washed in PBT for 3 x 15 minutes. To block non-specific binding sites the brains and VNCs were pre-incubated in 10% Normal Goat Serum (NGS) in PBT (blocking buffer) overnight at 4°C. The primary antibodies (see Table 3) were diluted in blocking buffer and this solution was then used to incubate brains and VNCs for 48 hours at 4°C. Next, the tissues were washed 3 × 15 min. in PBT and, then incubated overnight at 4°C (or for 3 hours at RT) with the secondary antibodies diluted in blocking buffer (see Table 3). After washing for 3 × 15 min. with PBT, the solution was replaced with Vectashield Antifade Mounting Medium (H-1000, Vector Laboratories, CA, USA) and the brains and VNCs were mounted on adhesion slides (Polysine slides, Thermo Scientific, Waltham, MA, USA). After covering the samples with Vectashield under a coverslip, the edges were sealed with nail polish and stored at 4°C until images were taken. Fluorescence images were acquired with a confocal laser scanning microscope (CLSM, Leica TCS SP8 WLL) via the Leica Application Suite X (LAS X, Leica Microsystems) using HC PL APO 10×/0.4, HC PL APO 20×/0.75 IMM objectives. Fluorescence signals were detected in serial stacks with a resolution of 1024 × 1024 pixels using 3 channels in sequential scanning mode. The GFP signal, which labeled the respective MN population of the GAL4 lines in Table 2 was acquired using an excitation laser wavelength of 488 nm and a HyD detector tuned to 498 – 540 nm. For Alexa Fluor 555 visualization, which was used to label the IPCs via the DILP2 antibody staining, we excited the fluorophore with the laser set to 555 nm and detected the emission with a PMT tuned to 565 – 620 nm. In the third channel, Alexa Fluor 635 bound to the nc82 antibody was excited with a wavelength of 633 nm and the emitted light was detected by a second PMT tuned to 643 – 693 nm. The image stacks were saved as a lif files from which maximum projections and scale bars were created using the Leica Application Suite X. Images were analyzed with ImageJ.

Table 3: Antibodies for anatomical receptor mapping, and brain and VNC anatomy

Antibody	Concentration	Reference or supplier
Primary		
Mouse anti-nc82	1:50	DSHB
Guinea pig anti-RFP	1:5000	Dr. Susan Brenner-Morton
Rabbit anti-DILP2	1:2000	Dr. Jan Veenstra (Veenstra et al., 2008)
Chicken anti-GFP	1:1000	Ab13970, Abcam, Berlin, Germany
Secondary		
Donkey anti-mouse Alexa 488	1:1000	ThermoFisher Scientific, Waltham, USA
Goat anti-guinea pig Alexa 555	1:1000	ThermoFisher Scientific
Donkey anti-rabbit Alexa 647	1:1000	ThermoFisher Scientific
Goat anti-chicken Alexa Fluor 488	1:200	ThermoFisher Scientific
Goat anti-rabbit Alexa Fluor 555	1:200	ThermoFisher Scientific
Goat anti-mouse Alexa Fluor 635	1:400	ThermoFisher Scientific

In vivo whole cell patch-clamp recordings

Fly handling and preparation were performed as described in (Ache et al., 2019). All experiments were performed at room temperature under daylight conditions. Before preparation, flies were cold anesthetized at 4°C for immobilization and the head and thorax were positioned in a custom-made shim plate fly holder and mounted with UV glue (Proformic C1001, VIKO UG, Munich, Germany). After removing the forelegs, the remaining stumps and the proboscis were glued together for maximal stability. Afterwards, a window was cut into the posterior cuticle of the head. Trachea, fat tissue, and the ocellar ganglion were removed to expose the brain and gain access to the IPC cell bodies in the pars intercerebralis (PI). The fly was then transferred with the fly holder into a fixed stage fluorescence upright microscope (Olympus BX51WIF, Olympus Corporation, Japan) or a customized Slicescope (Scientifica, Uckfield, UK). Live images of the fly brain were acquired with a high-resolution camera (SciCam Pro, Scientifica, US) using an image acquisition software (OCULAR, Digital Optics Limited, Auckland, NZ). The brain was continuously perfused with carbonated (95% O_2 and 5% CO_2) extracellular saline containing 103 mM NaCl, 3 mM KCl, 5 mM N-[Tris(hydroxymethyl)methyl]-2-aminoethanesulfonic acid, 10 mM D-(+)-glucose, 8 mM D-(+)-Trehalose dihydrate, 26 mM $NaHCO_3$, 1 mM NaH_2PO_4, 1.5 mM $CaCl_2.2H_2O$, 4 mM $MgCl_2.6H_2O$, and osmolarity adjusted to 273-275 mOsm (Gouwens & Wilson, 2009) during the preparation and the experiment. For enzymatic dissociation of the neural sheath from the brain above the IPCs, 0.025 % (w/v in extracellular saline) collagenase (Sigma-Aldrich #C5138) was applied locally in the PI region using a blunt thin-walled pipette. After identifying the GFP-expressing IPC cell bodies, whole cell patch-clamp recordings were performed using thick-walled patch pipettes (4 – 8 MΩ resistance) containing intracellular saline (140 mM potassium aspartate, 10 mM HEPES, 1 mM EGTA, 4 mM MgATP, 0.5 mM Na_3 GTP, and 1 mM KCl, adjusted to 260–275 mOsm, pH 7.3). Continuous time series of the membrane potential and spike events were captured in current clamp mode with an AxoPatch MultiClamp 200B (Molecular Devices LLC., San Jose, CA, USA). A part of data were also collected with a MultiClamp 700B amplifier (Molecular Devices). All data were recorded with a Digidata 1440A analog-digital converter (Molecular Devices) controlled by the pCLAMP 10 software using a 10 kHz low-pass filter and a 20 kHz sampling rate.

All optogenetics experiments were carried out using a 625 nm LED adjusted to an intensity of ~4.4 mW/cm^2 at the fly for CsChrimson activation. The LED was operated using TTL triggers controlled by preset protocols in pCLAMP. Each recording consisted of 10 activations with a stimulation length of 100 ms and a 10 s inter-stimulus-intervals. The TTL triggers were recorded simultaneously with the membrane potential and stored in abf format (Axon Binary File).

In vivo calcium imaging

Calcium imaging experiments were preceded by the same preparation protocol as for whole cell patch-clamp recordings. The calcium concentration of the extracellular saline solution was increased to match the saline used for calcium imaging used before (Seelig & Jayaraman, 2015), with a final concentration of 2.5 mM $CaCl_2.2H_2O$ All calcium imaging data were acquired with a Prime BSI Express Scientific CMOS camera (Teledyne Photometrics, Tucson, AZ, USA) in an *in vivo* fluorescence microscope (SliceScope, Scientifica) controlled by the ImageJ based software Micro-Manager 2.0 (Edelstein et al., 2014). Time series were recorded in a single z-plane at a framerate of 10 Hz for 2 min per trial and stored as tiff stacks. The x and y dimensions of the image frames were adjusted individually to the respective position of the IPCs in each fly. The genetically encoded calcium indicator GCaMP6m (Chen et al., 2013) was expressed in IPCs, while CsChrimson was expressed in the respective MN driver line (see Table 2). GCaMP6m was then excited via a tunable LED (pE-4000 universal fluorescence illumination system, CoolLED Ltd., Andover, UK) set to 470 nm. The light beam was directed through a GFP filter set (Chroma, Bellow Falls, VT, USA), including a 495 nm long-pass filter and an excitation filter with a bandwidth of 450-490 nm. An emission filter with a bandwidth of 500-

550 nm blocked unspecific background light before emitted light from the specimen was detected by the sCMOS sensor of the camera. CsChrimson was activated in the same manner as in patch-clamp recordings, but the activation protocols were adapted to the 2 min trials. The LED trigger signal was stored together with a trace of TTL pulses for each frame of the camera as abf files. We used different lengths of activation: 5 x 100 ms, 5 x 1 s, 2 x 5 s, or 1 x 15 s per time series, with the 5 s protocol being used for the majority of the analysis and figures.

Data Analysis

Single-nucleus transcriptomic analysis of IPCs

The pre-processed single-nucleus transcriptome data for IPCs was downloaded from https://www.flycellatlas.org/ (Li et al., 2022). This data was further processed and analyzed with the Seurat package (version 4.1.1; https://satijalab.org/seurat/articles/pbmc3k_tutorial.html) in R-Studio (Hao et al., 2021). The original data comprised of 658 single cell transcriptomes, derived from 250 males and 250 females, and sequenced using the Smart-seq2 technology. We used a stringent criterion (*Ilp2* > 0 & *Ilp3* > 0 & *Ilp5* > 0) to retrieve 392 IPC transcriptomes (from 194 male and 198 female flies transcriptomes) which express all three *Ilps*. Standard commands in Seurat were used to perform the t-distributed Stochastic Neighbor Embedding (t-SNE) analysis and create dot plots and feature plots. Heatmaps were generated using the heatmap package (1.0.12).

Patch-clamp

For patch-clamp recordings, all analysis steps and figure creations were carried out using custom-written MATLAB scripts (Mathworks, Natick, USA). To analyze the recorded patch-clamp traces we first detected all spike events using a custom-written function. To remove high-frequency noise from the traces, a median filter was applied using a time window of 250 ms to each of the 10 time series that compose an optogenetic stimulation experiment. We centered all values around zero by subtracting the median of each trace and we calculated the median of all 10 recordings to estimate the global response of each cell across trials. In order to provide a measure of the baseline activity variability, the 10th and 90th percentiles of all 10 filtered traces were computed in a time window of 900 ms starting 100 ms after recording onset. Thus, we established two thresholds to evaluate the effects of MN populations on the IPC activity. The median of the 10 traces was then used to represent the global response of the recorded IPC, and for the clustering into excited, inhibited, and non-responsive neurons. If the median trace was above the 90th percentile in a time window of 1 s starting at activation onset for longer than 50 consecutive milliseconds, the cell was classified as "excited". Conversely, an IPC was classified as "inhibited" if its activity was below the 10th percentile for 50 consecutive milliseconds, and as "no effect" if neither of the above cases applied. We ran this analysis across all recorded IPCs and across all tested activation experiments. Thus, we quantified the percentage of IPCs that were excited, inhibited, or unaffected by the activation of each MN population.

To further analyze the spiking activity, we computed the firing rate of each IPC across the 10 trials using non-overlapping time bins of 250 ms. To obtain an overall representation of the population response across all cells, we computed the mean of the median traces of all recorded cells and the mean of their individual firing rates, providing an overview of the collective neuronal activity during the activation experiments. The latency analysis of postsynaptic potentials was conducted using a Savitzky-Golay filter of 4th-order polynomial with four distinct time windows (400 ms, 200 ms, 100 ms, 50 ms) to capture fast dynamics of IPC activity while filtering out individual action potentials. After individual trial traces were filtered, we subtracted the median of each time series to center them to zero. We calculated the median of all 10 recordings and determined the 10th and 90th percentiles of baseline activity, following the previously described procedure for each time window. For cells previously classified as "excited" or "inhibited" we determined the latency of the stimulus as the time delay, following stimulus onset, at which the median of all 10 trials crossed the superior threshold (for excitation) or the inferior threshold (for inhibition). To estimate the overall latency, we averaged the values obtained from the four filter window lengths for each cell. Finally, to compare the magnitude of the IPC modulation via different modulatory populations, we computed the area under the curve (AUC) of the median traces with a trapezoidal numerical integration from activation onset to 1 s after onset. In the same manner, we calculated the baseline AUC from 1 s before stimulus onset to onset and then compared both values, p-values were calculated using the Wilcoxon signed-rank test. To compute a simple effect coefficient, we averaged the AUCs across all IPCs for the respective driver line, which indicated the activation shift of the population activity towards excitation or inhibition. By normalizing them to 1, with 1 being the maximum AUC value across all excited cells of the respective driver line, we were then able to compare the effects between activation experiments.

Calcium imaging

The pre-processing of all calcium imaging data was carried out with custom-written Python code based on the fly2p module as described before (Liessem et al., 2023). To pre-process the imaging data, each frame of a trial was spatially filtered with a two-pixel-wide Gaussian filter and x/y motion corrected by using phase correlation to a reference image that was generated from the mean over 50 frames in midst of a trial. Fluorescence changes were computed as $\Delta F/F = (F-F0)/F0$ for each pixel over all frames, with F0 being defined as fluorescence baseline averaged over the 10% of lowest-intensity frames in each trial. Next, individual IPC cell bodies were manually delimited as regions of interest (ROIs). From these ROIs, mean ΔF/F values were calculated throughout the time series by averaging pixels within the ROI, and stored as csv files. All further analysis steps were conducted using custom-written MATLAB scripts. First, the ΔF/F traces were aligned and visualized with the respective LED trigger signal. The distribution of the ΔF/F values of all ROIs was calculated in a 5 s window before the first stimulus across all 4 trials for each animal as a baseline. The ΔF/F traces for each ROI from 5 s before stimulus onset to 5 s after stimulus cessation were then superimposed and the mean of these traces was calculated. The mean ΔF/F traces for each IPC across all animals tested in the respective driver line were then visualized in a heatmap, normalized to the highest ΔF/F as 1 for each animal. To analyze the effect of each MN population on the IPC activity further, we employed a threshold-based clustering analysis. To this end, we calculated the individual 20th and 80th percentiles of the ΔF/F value distributions in the baseline window for each animal and each IPC separately and used them as upper and lower thresholds. If the ΔF/F trace rose above the upper threshold for a continuous frame number equal 25% of all frames in a window after stimulus onset until 5 s after stimulus offset, this IPC was classified as "excited". If the trace decreased beneath the lower threshold for the same time window, the IPC was classified as "inhibited". If an increase or decrease did not meet the time criteria or if the trace stayed between the thresholds, the cell was classified as "unaffected". Afterwards the mean and standard deviation were calculated for each cluster and each tested driver line. Then, we quantified the percent of IPCs per cluster based on the total number of IPCs recorded in every animal. To quantify how the activation of the respective modulatory neurons shifted the population activity of the IPCs, we also calculated an effect coefficient. To this end, we first subtracted the median of a 1 s baseline window before the stimulus onset from the ΔF/F traces and then calculated the area under the curve (AUC) as described for patch-clamp experiments for each ROI, from activation onset to 5 s after activation offset. Finally, we compared the AUC values of the traces without baseline subtraction in a 5 s time window before activation onset to the AUC values in a time window spanning from activation onset to 5 s after activation ceased. These two values were statistically compared, p-values were calculated using a Wilcoxon signed-rank test.
Finally, all figures were finalized with CorelDRAW (Cascade Parent Limited, Ottawa, Canada)

Table 4: p-values for calcium imaging AUCs before and after activation

Line	p-values			
	Global	**Excited**	**Unaffected**	**inhibited**
AstAN	< 0.0001	< 0.0001	0.6875	0.0078
OAN	< 0.0001	< 0.0001	0.9101	< 0.0001
DAN	0.0036	< 0.0001	0.0195	0.0001
LKN	0.3684	< 0.0001	0.0495	< 0.0001
MSN	< 0.0001	0.1562	0.3593	< 0.0001